CHAPTER 12

Auger Electron Spectroscopy of Target Atoms

B. Sulik* and N. Stolterfoht†

An introduction into the Auger process is presented including basic concepts, notation, classification and a brief history of target Auger spectroscopy studies in ion-atom collisions. Experimental methods and apparatus relevant for the field of target Auger spectroscopy are reviewed. Emphasis is given to the electron spectrometers including concrete realizations. Selected experimental studies are surveyed to illustrate the potentials of the experimental methods and provide insight into the trends in the field. The treated topics are multiple ionization of target atoms, angular distribution of the Auger emission, and post-collision interaction studies.

12.1 INTRODUCTION

The Auger process is a spontaneous decay mode of highly excited atoms or ions by electron emission. It competes with the well-known radiative decay. Since the observation of the process by Pierre Auger [1,2] in 1925 and the subsequent theoretical formulation by Wentzel [3] in 1927, the Auger effect has received increasing attention in many fields including atomic physics, nuclear physics, solid state physics, surface physics, and chemistry.

The transition resulting in Auger electron emission is caused by the electron-electron interaction. Generally, the Auger process involves two active electrons interacting with each other in the field of the atomic nucleus screened by the other (passive) electrons. The initial state is discrete and its energy lies above the first ionization threshold. The final state implies the ejected electron and the residual ion. When the Auger transition takes place in the isolated

*) Institute of Nuclear Research of the Hungarian Academy of Sciences (ATOMKI), P.O. Box 51, H-4001 Debrecen, Hungary.
†) Hahn-Meitner Institut Berlin GmbH, Bereich Festkörperphysik, Glienickerstr. 100, D-14109 Berlin, Germany.

atom, it depends only on the atomic properties. Therefore the study of the Auger effect yields direct information about the structure and the dynamics of the atom. For non-isolated atoms, the Auger process is rather sensitive to the surrounding electronic structure, which makes it widely applicable in chemistry and surface analysis.

To prepare the initial state one needs to create an inner-shell or core vacancy in the investigated atom or ion by means of photon, electron or ion/atom impact. Then absolute or relative Auger production cross sections can be determined from the measured line intensities. From these data cross sections for populating particular initial states can be derived, providing detailed information about vacancy production mechanisms like collisional excitation, ionization or electron capture.

It should be realized that the Auger process is relatively slow in comparison to time scales characteristic of the atom. For instance, the Auger process takes place during several hundreds of revolutions of orbiting outer-shell electrons. Thus it follows from the uncertainty principle that the natural spread of the Auger electron energy is small in comparison with the characteristic atomic energies. On the other hand, in comparison with the radiative transitions in outer shells, the Auger process is very fast and, hence, the corresponding width of the Auger lines is comparably large.

Moreover, the lifetime of the Auger or autoionization states is usually much longer than the atomic collision times. This is generally true for incident protons or electrons. For energetic ions, let us consider a collision where the projectile velocity is equal to the mean orbital velocity of the inner-shell electron to be ionized. Then it is reasonable to take the effective collision time equal to the time of one orbital revolution of the inner-shell electron. This yields an Auger lifetime several hundred times longer than the collision time. When reducing the projectile velocity by a factor of 10, the Auger lifetime still remains several tens of times longer. Therefore, a separate treatment of the vacancy production process and the Auger process is a reasonable approximation.

In the present chapter, high resolution Auger electron spectroscopy of target atoms is considered for energetic ion-atom collisions. A brief history and a short analysis of the specific features of target Auger spectroscopy is presented on an introductory level. Emphasis is given to the experimental method and apparatus. Finally, a few experimental studies have been selected to illustrate the potentials of the methods and give an impression about the tendencies in the field.

The separate treatment of target spectroscopy and projectile spectroscopy in this book reflects the historical fact that they have developed rather separately from the early 1970's. Projectile Auger spectroscopy and the related instrumental aspects are detailed in the forthcoming two chapters of the present book.

For a wider overview of the field of target Auger spectroscopy, the reader is

referred to the comprehensive articles that review the work about the Auger effect. The theory of autoionization and the Auger effect has been discussed in detail by Burke [4], Burhop and Asaad [5] Chattarji [6], McGuire [7], Åberg and Howat [8], and Stolterfoht [9] . Atomic structure calculations related to Auger line energies and transition probabilities are widely referred e.g., in the review of Stolterfoht [9] and in a recent paper of Kabachnik *et al.* [10].

Surveys about experimental studies of ion-induced Auger electrons have been given by Ogurtsov [11], Niehaus [12], Rudd and Macek [13] Sevier [14], Mehlhorn [15–17], Matthews [18], Berényi [19,20] and Stolterfoht [9,21,22]. Some of them [16,20–22] cover both target and projectile Auger spectroscopy. Specific experimental studies of electron spectra have been discussed by Stolterfoht [23–25], Berényi [19], Mann *et al.* [26] and Rudd *et al.* [27]. Related work concerning excitation mechanisms in ion-atom collisions have been reviewed, e.g., by Garcia *et al.* [28], Kessel and Fastrup [29], Meyerhof and Taulbjerg [30], Briggs and Macek [31], and McGuire [32].

Target Auger studies by electron and photon impact have been surveyed e.g., by Siegbahn *et al.* [33], Krause [34], Carlson [35], and Mehlhorn [15–17]. Application for chemistry and surface analysis is detailed in the works of Siegbahn *et al.* [36] and Riviere [37]. Electron emission from slow atomic collisions has been overviewed by Niehaus [38].

In the following, we restrict our considerations to the high-resolution Auger spectroscopy of free atoms, i.e., gas or vapour targets, at the beamlines of heavy particle accelerators. The impact energy region is larger than a few tenth of keV/u. Throughout this chapter atomic units ($m_e = e = \hbar = 1$) are used unless otherwise stated.

12.1.1 Brief history

In the early 1960's, electrostatic electron spectrometers became widely used in studies of the Auger effect and autoionization at gaseous or vapour targets by electron and photon impact (see e.g., refs. [39–42]). The high resolution abilities of the spectrometers made possible a detailed analysis of spectral structures.

The first use of energetic ions to obtain spectroscopic information about Auger and autoionization states started in 1964. Rudd [43] measured the first high resolution spectra of He autoionization electrons produced by H^+ and H impact. The use of incident ions has advantages compared to photon and electron impact, since they may excite states which are otherwise not accessible. However, the use of ions has also disadvantages. Ion impact produces line broadening which may inhibit high-resolution studies. The decaying target atom may be influenced by the slowly emerging charged projectile producing the post-collision effect. It was first observed by Barker and Berry [44] in early experiments of ion-induced autoionization electrons. Moreover, line broadening is produced by kinematic effects [9,45]. In particular, heavy ions transfer

large recoil momenta so that the emitter moves in different directions during the decay [46]. For example, the lines in the Ne K Auger spectrum cannot be resolved when they are produced in Ne + Ne collisions at energies of a few hundred keV [47].

For the target atom, broadening effects can be reduced substantially when the impact energy is increased. In 1973 Ne-Auger spectra were measured with high resolution by Matthews *et al.* [48] using oxygen projectiles of about 30 MeV. The spectra confirmed previous observations in the field of X-ray spectroscopy which have indicated considerable outer-shell ionization in addition to the inner-shell vacancy production [49]. In fact, with very heavy projectiles, the target atom can be stripped to a few-electron system as shown by Stolterfoht *et al.* [50] for 200-MeV Xe^{31+} projectiles.

The possibility of removing several electrons in a single collision and reducing the kinematic broadening effects opened the field of high-resolution Auger spectroscopy of few electron systems. Several groups performed studies of target Auger electron produced by energetic heavy-ion impact (see e.g., Matthews *et al.* [48], Schneider *et al.* [51], Mann and Folkmann [52], Woods *et al.* [53], Kádár *et al.* [54], and Matsuo *et al.* [55]).

By varying the charge state of heavy projectiles in fast collisions, different degrees of multiple ionization of the same target species can be achieved. From the set of high-resolution spectra, a large portion of satellite lines associated with different initial vacancy states can be identified. With this method, 2s and 2p subshell ionization probabilities or full subshell vacancy population distributions associated with K-shell ionization of Ne were determined by Kádár *et al.* [56,57] and Sulik *et al.* [58] in 5.5 MeV/u H^+, N^{2+}, N^{7+}, Ne^{3+}, Ne^{10+}, Ar^{6+}, Ar^{16+} + Ne collisions. This kind of experimental study is valuable for understanding the mechanism and the statistical aspects of multiple vacancy production in heavy ion-atom collisions.

Finer details of the excitation or multiple ionization dynamics can be experimentally studied by measuring the angular distribution of the emitted Auger electrons. The observed anisotropy of the Auger lines provides information about the non-statistical population of the magnetic electron or vacancy substates, i.e., the alignment of the charge cloud, in the collision. The anisotropy of the Li $1s2s2p\ ^2P$ lines excited by 50-400 keV H^+ and He^+ projectiles was studied and interpreted by Ziem *et al.* [59]. The first evidences of nonstatistical population and anisotropic satellite distribution in multiply ionized neon were provided by Matthews *et al.* [60] and Stolterfoht [23]. The first experimental determination of the anisotropy parameters for satellite Auger lines in the spectrum of neon, doubly ionized by 5.5 MeV/u heavy ions, was reported by Ricz *et al.* [61,62]. These data triggered a long discussion in atomic structure theory [10]. By coincidence methods, Sarkadi *et al.* [63] and Gutenkunst *et al.* [64] separated the electron capture and ionization contributions to the vacancy production on the L_3 subshell of argon and magnesium by proton bombardment. A strong alignment with steep impact velocity dependence

has been found for the capture process in both cases, while the integral alignment was nearly zero. The observed impact velocity dependence has been reproduced only qualitatively by capture theories.

Detailed information about the post-collision interaction (PCI) of the outgoing Auger electrons with other collision fragments can be extracted from high-resolution Auger spectra by analyzing the shape of the individual lines. Under ion impact, PCI is a rather complicated effect with strong impact velocity and angular dependence. Systematic studies have been performed on this topic by Arcuni [65], Takács *et al.* [66], Sarkadi *et al.* [68], and Ricz [67].

It is worth mentioning here that both PCI and angular distributions are widely investigated by electron impact (see e.g., refs. [69–71]). Auger studies on atomic and molecular species at synchrotrons have also been reported recently (e.g., refs. [72,73]). Systematic work on target species by merging the potentials of the accelerator, electron-impact and synchrotron facilities together, could be a future trend in atomic physics.

12.2 THE AUGER EFFECT

In a simple picture, the Auger effect may be regarded as electron transitions between atomic orbitals shown in Fig. (12.1). The example refers to a vacancy in the shell A being filled by an electron from the shell B. The excess energy is given to an electron in the shell C so that it is transferred to a continuum state of well-defined energies.

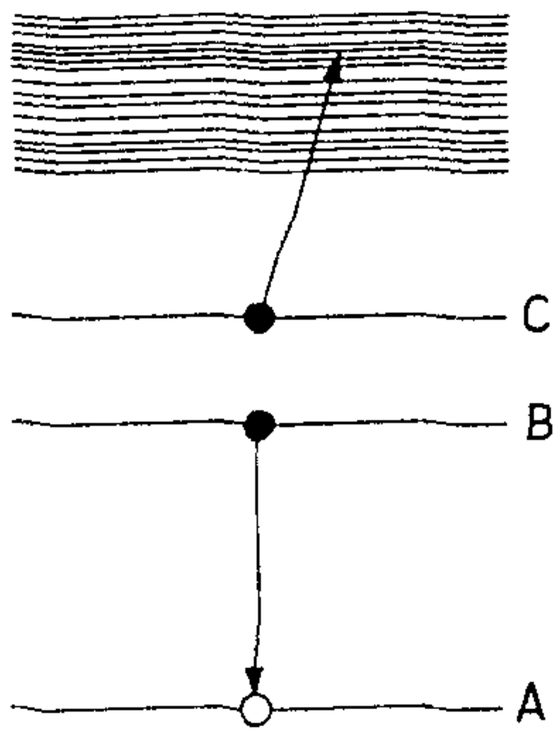

FIGURE 12.1 Schematic diagram illustrating the Auger effect

The spontaneous transition causing the emission of an electron is also called autoionization. In principle, there is no difference between the Auger effect and autoionization. However, for historical reasons it is common use to distinguish between different categories of initial states. The Auger effect refers to atoms ionized in an inner shell whereas autoionization is attributed to atoms doubly excited in the valence shell. However, it should be emphasized that

this distinction loses significance when inner and outer shells are simultaneously excited or ionized. In the following, the notation Auger effect is used to cover both effects.

An individual Auger transition is defined by specifying fully the initial and final states involved. In multi-electron systems it is convenient to consider vacancies rather than electrons [74]. For example, an individual Auger transition is denoted by K-$L_1L_{23}(^1P)$, where the LS-coupling scheme is applied to fully specify the final state. Also, the transition K-$L_1L_{23}(^3P)$ may be considered. Each transition gives rise to a line in the corresponding Auger spectrum as shown in Fig. (12.2). The example refers to the K-Auger spectrum of Ne excited by 4.2-MeV H^+ impact [75].

All individual Auger transitions possible for given (sub)shells are summarized to (sub)groups using the notation K-L_1L_{23} or K-LL for example. Similarly, groups are summarized to series where only the shell of the initial state is specified, e.g. K-series or L-series. The present notation may also be applied to multi-vacancy states often created by heavy particle impact. Suppose that n L-vacancies are initially produced in addition to the K-vacancy, one may write KL_n-L_{n+2}. Of course, also subshells as well as terms may be specified.

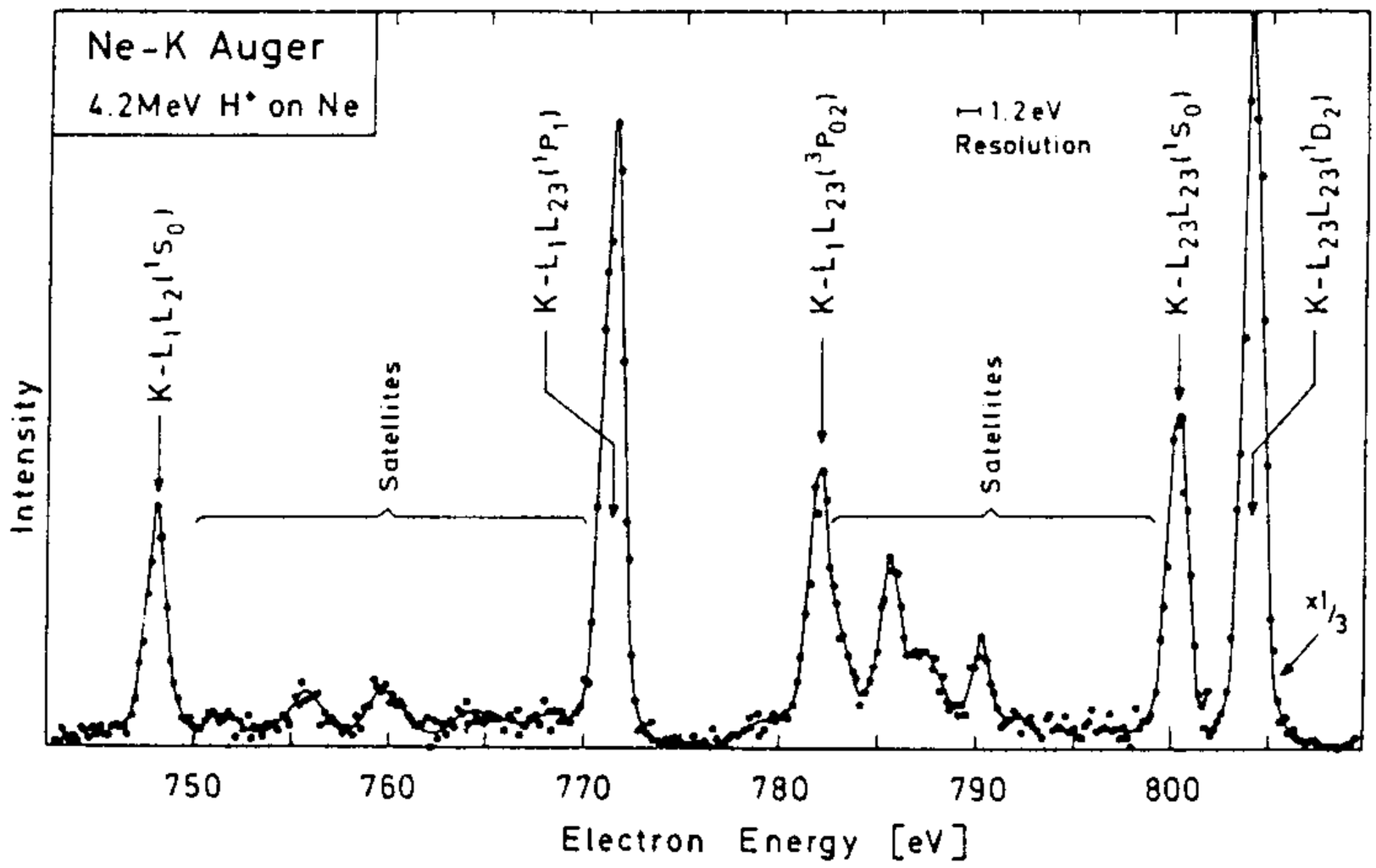

FIGURE 12.2 Neon-K Auger spectrum produced by 4.2-Mev/u H^+ impact. Reprinted from N. Stolterfoht, H. Gabler and U. Leithauser, "High-resolution Ne Auger spectrum produced in 4.2 MeV H^+ - Ne collisions." [75], with kind permission of Elsevier Science - NL, Sara Burgerhartstraat 25, 1055 KV Amsterdam, The Netherlands.

An Auger line which refers to the transition from a single vacancy state to double vacancy states is denoted a normal line or *diagram line.* Other lines are called *satellites.* For instance, the lines attributed to initial multi-vacancy states are satellites. Furthermore, lines due to double vacancies initially in the inner shell are called *hypersatellites.* The distinction between normal lines

and satellite lines is very useful for incident electrons, photons and light ions, which produce primarily initial single vacancy states. However, for heavy ions which produce primarily multi-vacancy states, this distinction loses significance. Very often, heavy ions produce Auger spectra which consist exclusively of satellite lines.

Auger transitions imply definite selection rules referring to the final state of the *total* system. The initial state and the final state are specified by the total angular momenta J_i and J_f and their magnetic quantum number M_i and M_f, respectively. In general, $\Delta J = 0$ and $\Delta M = 0$ for the Coulomb, spin-orbit and spin-spin interactions. Only the hyperfine interaction can change them by ± 1. Parity is always conserved, $\Delta \Pi = 0$. The total orbital momentum L and the total spin S are conserved only for the Coulomb interaction.

Further notations are commonly used to classify the Auger effect. A transition is called a Coster- Kronig (CK) transition [76] when the initial vacancy and one final vacancy occupy subshells within one shell. If the initial vacancy and both final vacancies are produced in the same principal shell, the transition is called Super-Coster-Kronig (SCK) transition. It is only mentioned here that higher-order Auger processes are also possible where three or more electrons are affected [12,42,77–81].

The Auger process is characterized by the transition energy which is defined as the difference between the energies of the initial state and the final ionic state. The transition energy is equal to the energy of the ejected electron. Furthermore, the Auger process is characterized by the transition rate P_{if} which is equal to the number of Auger transitions per unit time. The transition rate corresponds by way of the uncertainty principle to the partial Auger width Γ^a_{if}, which has the dimension of energy. Actually, the quantities P_{if} and Γ^a_{if} are equal in magnitude in atomic units. It should be pointed out that the transition rate as well as the transition energy are defined for isolated atoms and, hence, they are typical atomic structure quantities.

If there are several Auger decay channels for a given initial state, the corresponding partial Auger widths add to the Auger width

$$\Gamma^a_i = \sum_f \Gamma^a_{if} \tag{12.1}$$

of the initial state. Analogously, the Coster-Kronig width Γ^{ck}_i and the radiative width Γ^x_i are obtained. These widths contribute to the total with

$$\Gamma_i = \Gamma^a_i + \Gamma^{ck}_i + \Gamma^x_i \tag{12.2}$$

of the initial state. Then it follows for the natural line width

$$\Gamma^n_i = \Gamma_i + \Gamma_{f'} \tag{12.3}$$

of an Auger line, where $\Gamma_{f'}$ is the total width of the final states which may further decay. The difference between the partial width Γ^a_{if} and the natural

line width Γ_i^n should be noted. The partial width Γ_{if}^a is uniquely specified by the initial and the final state, whereas Γ_i^n depends on transitions other than from i to f and/or on radiative transitions.

The branching ratio into a specific Auger channel is the partial Auger yield

$$a_{if} = \Gamma_{if}^a / \Gamma_i \tag{12.4}$$

The decay in all Auger channels defines the Auger yield

$$a_i = \Gamma_i^a / \Gamma_i \tag{12.5}$$

Similarly, the Coster-Kronig yield f_i and the fluorescence yield ω_i are obtained. From eq. (12.2) it is seen that

$$a_i + f_i + \omega_i = 1.$$

Information about the widths and yields are obtained from the related line spectra. A transition from an initial state to a final state gives rise to a specific line whose intensity I_{if} is a measure for the corresponding excitation probability and branching ratio.

It is important to realize that the Auger line intensity is not proportional to the transition rate P_{if}, but it is proportional to the Auger yield a_{if}. Often, a_{if} is close to unity, i.e.,, when the decay to one final state f dominates. In this case, the intensity I_{if} probes primarily the excitation probability Q_i. Information about the transition rate P_{if} may then be obtained from the analysis of the natural width of the Auger line.

Neither the theory of ion-atom collisions nor that of the Auger effect will be discussed here. Comprehensive works have been reported in Section 12.1. From an experimental point of view, however, it is important to provide a general picture about the energy and angular distribution of the electrons emitted in the Auger process, i.e., about the differential Auger production cross sections.

For fast projectiles, the collision and the Auger decay can be treated as successive, independent processes. Then the single differential Auger emission cross section for a particular Auger transition $i \rightarrow f$ (i.e., a particular Auger line) is written in the factorized form [8]

$$\frac{d\sigma}{dE} = \frac{\Gamma_{if}^a / 2\pi}{(E - E_a)^2 + (\Gamma_i^n / 2)^2} \, \sigma_i \, . \tag{12.6}$$

Here E_a is the nominal energy of the Auger transition $i \rightarrow f$, while σ_i is the production cross section of the initial state i for the collision. Eq. (12.6) provides a symmetric Lorenzian line-shape characterized by the natural line-width Γ_i^n.

A similar factorization can be achieved in the description of the angular distribution of the Auger electrons in non-coincidence measurements [16]

$$I(\Theta) = \frac{I_0}{4\pi}\left(1 + \sum_{k=2}^{k_{max}} \alpha_k A_{k0} P_k(\cos\Theta)\right), \tag{12.7}$$

where the parameter α_k depends only on the Auger process, while the alignment parameter A_{k0} is determined exclusively by the relative populations of the magnetic substates in the collision process. The total Auger intensity I_0 is an integral over the solid angle. The $P_k(\cos\Theta)$ are Legendre polynomials and Θ is the polar angle relative to the beam direction. The index k runs over the even numbers. In simple systems, k_{max} is a small number, e.g., for single electron or single vacancy initial states on the L_{23} subshell, $k_{max} = 2$.

It is noted that replacing I_0 by $d\sigma/dE$ (from Eq. (12.6)), Eq. (12.7) directly yields the double differential Auger electron emission cross section, provided σ_i represents the sum of the magnetic substate population cross sections.

The above formulas show general symmetries in the Auger electron emission, i.e., a symmetry in the line-shape and a forward-backward symmetry in the angular distribution. This fact originates from the separate treatment of the collision process and the Auger process. Any asymmetry observed in the experimental data indicates that this separation is not justified for the system studied.

12.3 EXPERIMENTAL METHOD AND APPARATUS

There are only a few studies covering the majority of the instrumental and methodological details relevant for the field of accelerator based target Auger spectroscopy (e.g., refs. [13,18,25]). Many related aspects, however, have been carefully analyzed in different papers (e.g., refs. [9,14,16,27,57,82–85]. In the present work, an attempt is made to *mention* all the important topics providing references, and summarize the basic knowledge for planning experiments and collecting data. Some instrumental developments are also reported in the present Section.

12.3.1 General considerations

Fig.(12.3) shows the schematic diagram of an experimental setup and the geometry of the collision region, typical for electron-spectroscopic studies at ion-beams impinging on a gas target. The arrangement is common for most non-coincidence experiments where secondary electrons are measured. At this stage, we try to minimize the applied approximations. An arbitrary density distribution of the target atoms $n(\mathbf{r})$ is considered. Similarly, the beam flux $n_b(\mathbf{r}_\perp)$ is allowed to vary arbitrarily in two-dimensions. Background counts as well as the scattering of the emitted electrons on the target gas are not considered here, since they can be treated separately.

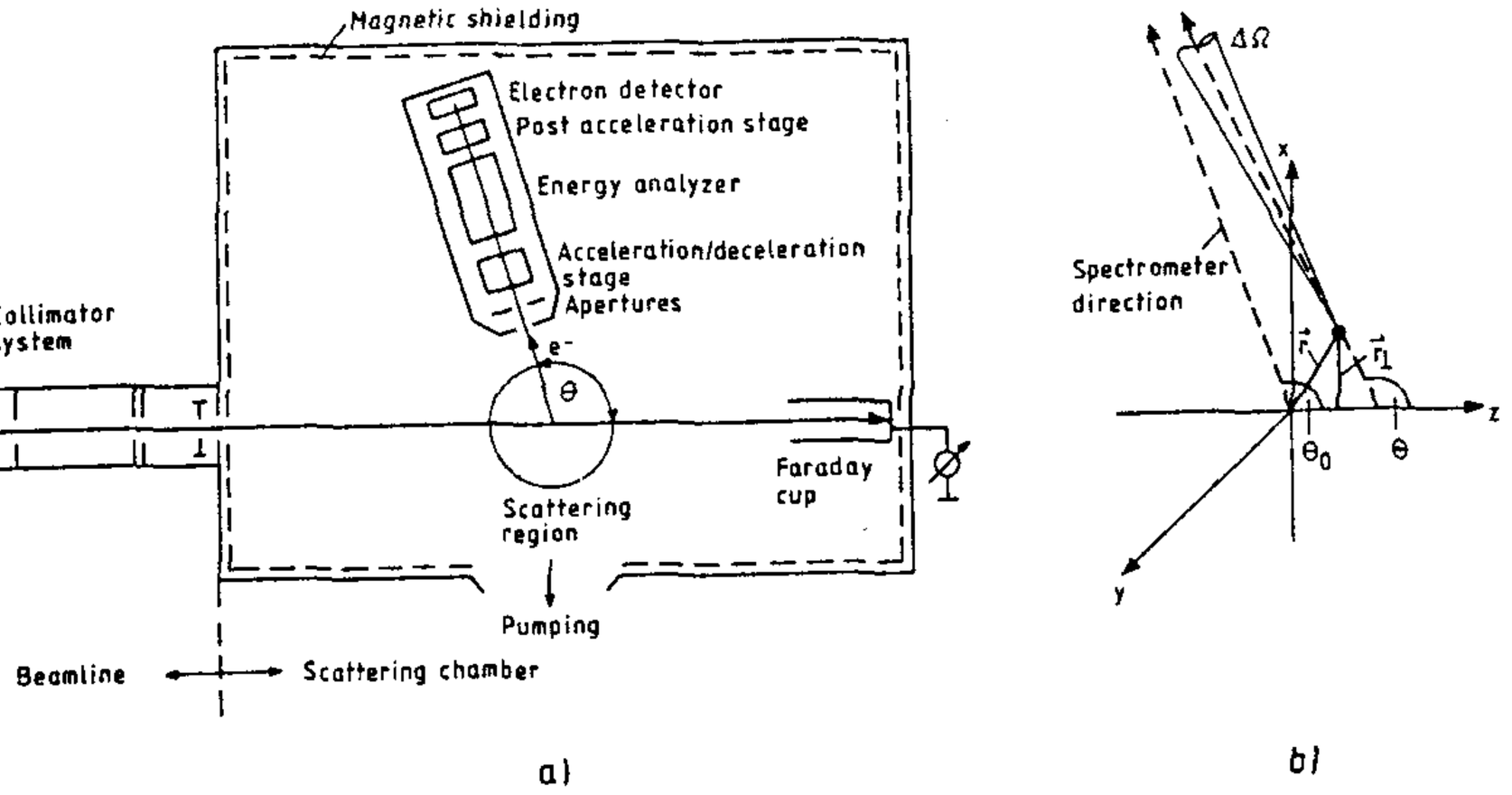

FIGURE 12.3 Typical experimental setup used for electron measurements in ion - gas atom collisions (a), and the geometry of the collision region (b).

The number of electrons counted at a nominal energy E_0 (set by the spectrometer voltages) and a nominal polar angle Θ_0 is as follows.

$$N_e(E_0, \Theta_0) = \int_{V,E} dV\, dE\, \frac{d^2\sigma[E, \Theta(\mathbf{r})]}{d\Omega\, dE}\, n(\mathbf{r})\, n_b(\mathbf{r}_\perp)\, \Delta\Omega(\mathbf{r})\, t(E, E_0, \mathbf{r})\, \eta(E) \quad (12.8)$$

Here E is the energy of the emitted electron, Θ is the polar angle of emission relative to the beam direction (z-axis) and $d^2\sigma/d\Omega dE$ is the double-differential cross section (DDCS) for electron emission in the collision process. The solid angle $\Delta\Omega$ is defined by the first slit (or object slit, see below in Fig. (12.5)) of the spectrometer. For monoenergetic electrons emitted with kinetic energy E from point $\mathbf{r}$, the inner part of the spectrometer is fully characterized by the dimensionless transmission function $t(E, E_0, \mathbf{r})$. In general, the efficiency of the electron detector $\eta(E)$ is also energy dependent.

The above picture may be used as a guide to the planning of a specific experiment. The quantities in Eq. (12.8) should be accurately measurable. Usually, reasonable approximations are made. The maximum value of $\Delta\Omega$ should be small compared to the angular variation of DDCS. Similarly, the energy region ΔE where the transmission t is nonzero should be narrow compared to the energy variations of DDCS. Then, it is justified to put the DDCS term in front of the integral. The detector efficiency is a slowly (if at all) varying function of E and can be considered as constant within the ΔE region.

In most experiments, the beam is well collimated into a small spot-size. Accordingly, the collision volume is small, and one does not need to know the distribution of the beam flux n_b, only the total flux N which is measured by a Faraday cup and current integrator. If the target is a gas-cell, the target density n is approximately constant and one has a homogeneous line target.

If the distance of the first slit (object slit, see Fig. 12.5 below) of the spectrometer from the collision region is large compared to the beam diameter and the object slit size, the transmission function of the spectrometer t can be factorized to separate $\mathbf{r}$-dependent and E-dependent terms. Consequently, the spectrometer is well characterized by an effective product of the solid angle and the target length $(l\Delta\Omega)_{eff}$ (depending on Θ), a maximum transmission T, and an effective energy window $\Delta E(E)$ [13,25].

Finally, the right side of Eq. (12.8) is obtained as a product and one gets the well known formula for the DDCS (see e.g., [27])

$$\frac{d^2\sigma(E,\Theta)}{d\Omega\, dE} = \frac{N_e}{N\, n\, T\, (l\Delta\Omega)_{eff}\, \Delta E\, \eta}\,, \tag{12.9}$$

which can be used in most cases. It is more advanced, however, to start from Eq. (12.8), and check the conditions of all the simplifying steps when planning an experimental setup. For non-homogeneous gas jet targets (see below) e.g., it is more appropriate to determine an effective quantity $(nl\Delta\Omega)_{eff}$ than to use the product $n(l\Delta\Omega)_{eff}$.

In general, the most difficult task is to measure absolute DDCS with reasonable accuracy. Instrumental and methodological aspects have recently been analyzed in detail by Rudd *et al.* [27]. In target Auger spectroscopy, the most important quantities to study are the line energies, relative line intensities, and line shapes. Therefore, in the following, we concentrate on relative measurements. Since the majority of the problems are common for absolute and relative measurements, some items are only mentioned or briefly treated here. For more details, the reader is referred to the recent review [27].

Particular aspects are characteristic of Auger spectroscopy. In order to achieve reliable spectroscopic information, e.g., the kinetic energy of the Auger electrons has to be measured with high absolute accuracy. Hence, the calibration of the energy scale as well as accuracy, and long-term stability are essential problems. Therefore, emphasis is given to these topics in the following discussion.

12.3.2 Gas targets and vacuum conditions

For typical gas target measurements, the scattering chamber is operated under high vacuum conditions yielding a base pressure of typically less then 10^{-6} mbar (without external gas inlet). Electron spectroscopy studies are generally performed under single collision conditions. Gas jet or gas cell targets have both been used in past.

The gas jet is usually a simple tube between 0.2-1 mm diameter operated at distances of a few mm from the ion beam. A gas jet is typically oriented perpendicular to the scattering plane defined by the beam and the spectrometer. A more directed gas beam can be achieved by using a bundle of narrower tubes. A common solution is to use a small piece of a microchannel plate,

where the diameter of the individual tubes is a few tenth of microns. The advantage of a more directed gas beam is that the target is more localized. Furthermore, a better ratio of the target-region pressure to the base pressure can be achieved by the same pumping power. With such gas jets, pressures of a few 10^{-3} Torr are typically obtained in the target region. Gas jets are simple and compact, leaving space around the collision region. However, they must be properly aligned even for relative measurements. The main disadvantage of them is that neither the value of the average target pressure nor the inhomogeneous density distribution of the target can readily be measured.

To obtain higher target pressures, differentially pumped gas cells may be used. Gas cell targets are better suited for absolute cross section measurements than gas jets, since the target density is constant in the collision region. Moreover, the target pressure may be directly measured. However, for electron DDCS measurements the cell should be prepared with many holes allowing the electrons to enter the spectrometer at different angles. It may be complicated to construct an adequate arrangement for differential pumping. Another problem is the scattering of both the ion beam and emitted electrons in the target gas within the cell. The latter causes not only a loss in the counting due to the electron absorption by the targer gas but also a scattering into other angular channels, distorting the measured angular distributions [13]. Furthermore, already small scattering on the walls or slits of the gas cell may easily produce a large number of stray electrons.

The gas pressure in the scattering center must be limited so that the electron detectors are not affected. Moreover, care must be taken to establish single-collision conditions. For instance, to preserve the incident charge state the projectile should not undergo charge-changing collisions. The probability W that a particle traveling through a gas region of length l and pressure P suffers a collision is [25]

$$W = \sigma \, l \, P \, c_v$$

where σ is the relevant total cross section and $c_v = 2.4\ 10^{16}$ 1/cm^{3}mbar is the constant converting the pressure of mbar into number of particles per cm^3. With a path length of 0.3 cm and a pressure of 4 10^{-3} mbar, typical for a gas jet, it follows that W is negligibly small ($\leq 10^{-2}$) if the cross section does not exceed the values of 10^{-15} cm^2 [25].

When the gas pressure is sufficiently low to fulfill the single collision condition, a large beam current can, in principle, produce space charging by ionizing a significant portion of the target gas along its trajectory [27]. This effect is more pronounced for heavy ion impact. Space charge yields line shifting and broadening, which makes it especially unpleasant in Auger spectroscopy. Unavoidable beam fluctuations may further increase broadening. To eliminate the effect, the beam current must be kept at a sufficiently low value, where the line positions are stable.

12.3.3 Electron spectrometers

For the energy analysis of electrons various types of electrostatic spectrometers are used. Generally, the theory of the electrostatic spectrometers is relatively complex so that only general aspects are discussed here. For more details the reader is referred to the articles by Rudd [13], Roy and Carette [86], Dahl [87], Wannberg *et al.* [88], Afanasjev and Javor [89], Granneman and Van der Wiel [90], Leckey [91], and Roy and Tremblay [92].

Fig. 12.4 shows different types of energy dispersive electrostatic spectrometers utilized in ion-atom collision experiments. Each spectrometer consists essentially of two plates producing a well defined electric field. The notations of the spectrometers refer primarily to the shape of the plates. There are the parallel plate spectrometer [93,94], the cylindrical plate spectrometer [95], the toroidal spectrometer [96–99], and its two simpler and widely used versions, namely the cylindrical mirror analyzer (CMA) [100,101], and the concentric hemispherical analyzer (CHA) [33] or its sector version, the spherical plate spectrometer [102]. It should be noted here that our aim is to provide brief information about the spectrometers most often used in ion-atom collision experiments. Different names for both the spectrometers and their parts can be found in the literature. Many authors prefer to use e.g., the word 'electrode' instead of 'plate' or 'plain mirror' instead of 'parallel plate'. For a more systematic classification, the reader is referred to Refs. [89,91].

It is rather common to make a distinction between spectrometer and analyzer in the literature. Usually, the analyzer is considered as the energy dispersive element of the spectrometer, which latter contains all the elements from the first aperture to the detector including accelerator/decelerator lenses. In this sense, Fig. (12.4) shows analyzers. The distinction, however, is not always unique. In the following we talk about spectrometers, but no acceleration/deceleration lenses are considered in the formulas. However, when the term 'analyzer' is included in a commonly used abreviation, e.g., CMA or CHA, both terms are used with the same meaning.

The deflection angle α_D is a characteristic parameter of any spectrometer. In Fig.(12.5) slit geometries and corresponding electron trajectories are shown for a parallel plate spectrometer with a deflection angle $\alpha_D = 60°$. (It is common to refer to this spectrometer by its entrance angle $\alpha_0 = 30°$). It is noted, however, that the following discussion deals with general aspects so that it applies to other spectrometers, too.

Electrons from the source enter the electric field through the entrance slit. After appropriate deflection the electrons leave the field by passing the exit slit. The slit denoted 'object' defines the beam of electrons before passing the entrance slit. Another defining slit denoted 'image' is located at the image of the object. The object and image may coincide with the entrance and exit slit, respectively. Let us denote the widths of the four slits by w_o, w_{ent}, w_{ex}, and w_i. The corresponding heights of the slits are denoted by h_o, h_{ent}, etc. On a plane perpendicular to the electron trajectories the projected effective width

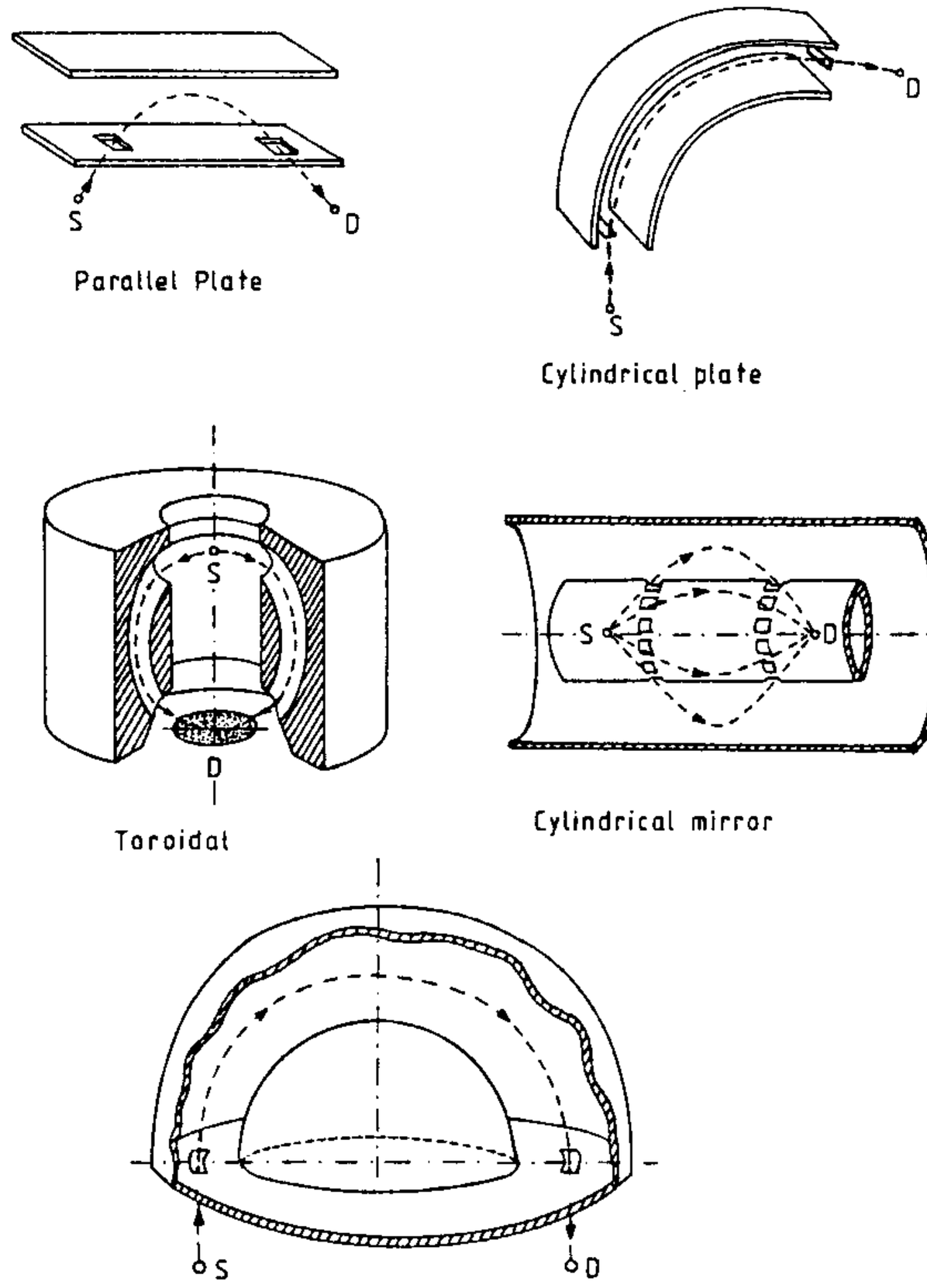

FIGURE 12.4 Different types of electrostatic electron spectrometers.

of the slits is smaller. It is useful to give an independent notation s_o, s_{ent}, etc., to the projected slit widths. In the specific case of $\alpha_D = 60°$, $s_x = \sin(30°)w_x$, i.e., $s_x = w_x/2$.

In the following, the angle measured in the plane of the electron trajectory (i.e., in the graphical plane of Fig. 12.5), α will be referred to as polar angle. The angle measured in the direction perpendicular to the plane of the electron trajectory, β will be referred to as azimuthal angle. To avoid conflicts, the notation of the polar and azimuthal angles relevant for the electron spectrometers (α, β) have been chosen to be different from those relevant for the collision system (Θ, Φ).

Let L be the distance between the crossing points of the electron trajectories with the object and image slits. For electrons originating from a point source the object slit determines the polar acceptance angle $\Delta\alpha_o = s_o/d_{so}$ where d_{so} is the source - object slit distance. One may define a different polar angle $\Delta\alpha_s$ from the opposite direction. The maximum value of $\Delta\alpha_s$ is the angular range

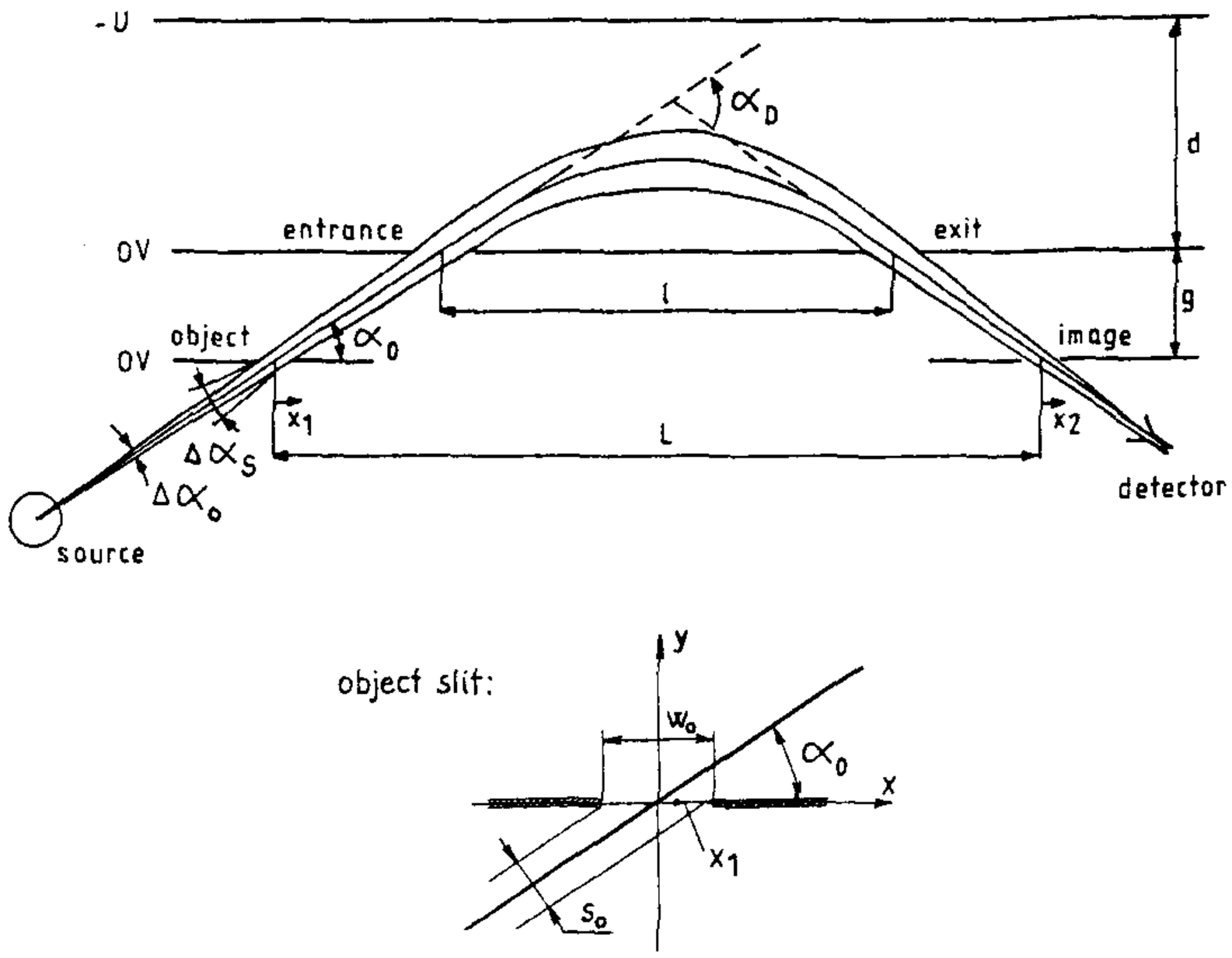

FIGURE 12.5 Geometry of a parallel plate spectrometer ($\alpha_D = 60°$).

of all the possible trajectories passing through the spectrometer, considered at the object slit. Hence, this maximum $\Delta\alpha_s$ determines the maximum source size in the polar direction. Electrons emitted outside this angular region cannot be counted. If, however, the source size is smaller, $\Delta\alpha_s$ is determined by the source size.

The maximum possible divergence of the electron beam with respect to the polar entrance angle α_0 is $\Delta\alpha = \Delta\alpha_o/2 + \Delta\alpha_s/2$. Let the analogous azimuthal quantities for the electrons (in the direction perpendicular to the electron trajectory plane) be $\Delta\beta_o$, and $\Delta\beta_s$, and the maximum azimuthal divergence $\Delta\beta$.

Now, it is possible to introduce some characteristic quantities of the spectrometer. The solid angle is obtained as $\Delta\Omega = \Delta\alpha_o\Delta\beta_o$. It is determined exclusively by the position of the (point) source and the geometry of the object slit of the spectrometer. Let us recall from Eq. (12.8) that, at a given position of a point source, the spectrometer between the object slit and the image slit is characterized by its transmission t. The product of the spectrometer transmission and the solid angle $\Delta\omega(\mathbf{r}) = \Delta\Omega(\mathbf{r})\, t(\mathbf{r})$ characteristic to a point source in an arbitrary position $\mathbf{r}$ can be considered as an effective solid angle.

The effective solid angle $\Delta\omega(\mathbf{r}_0)$ characteristic of a point source in its *central* position is often referred to as *brightness*. Varying the position of the point source in the vinicity of its central place, $\Delta\omega$ becomes smaller. The

accepted area of the source can be estimated as $(d_{so}\Delta\beta_s + h_o)(d_{so}\Delta\alpha_s + w_o)$. Averaging over this area, a mean effective solid angle $\overline{\Delta\omega}$ can be determined ($\overline{\Delta\omega} < \Delta\omega(\mathbf{r}_0)$). For extended sources, the measure of the efficiency of the spectrometer is the *luminosity* which is equal to the product of the mean effective solid angle and the accepted area of the source.

In ion-atom collision experiments, the source area is the product of the length l and the diameter of the beam seen by the spectrometer. In most cases, the beam diameter does not appear explicitly in Eq. (12.9), but it is implied in the beam current $J = N/t$. The beam current usually increases when the beam diameter increases. Hence, the luminosity of the spectrometer enters into Eq.(12.9) through the quantities $(l\Delta\Omega)_{eff}$ and N. This shows that for a given resolution the spectrometer with large luminosity is favored, as a high count rate is desirable.

Both the solid angle and the accepted source area are determined by the focusing power of the spectrometer. The most important focusing parameters and the energy resolution of a spectrometer are determined by the function $x_2(x_1, \alpha, \beta, E)$ which gives the position of the electron trajectory at the image slit, as a function of its position and direction at the object slit and the kinetic energy of the electron. The explicit expression of x_2 is called the basic equation of the analyzer (see e.g., [13]). The Taylor expansion of x_2 up to first order in energy and up to the first nonvanishing angular terms has a unique form for electrostatic spectrometers [13,82]

$$x_2 = M\, x_1 + D\, \frac{E - E_0}{E_0} + P\, (\alpha - \alpha_0)^n + A\, (\beta - \beta_0)^m, \qquad (12.10)$$

where $m, n \geq 2$. The quantities with index '0' are the nominal values belonging to the central electron trajectory ($x_1 = x_2 = 0$). The nominal energy of the spectrometer E_0 is determined by the electrode potential U and geometric factors. The geometric ratio $c = U/E_0$ is denoted as *spectrometer constant.*

The expansion parameters in Eq. (12.10) have special meanings. For spectrometers without acceleration or deceleration between the object and image slits, the *magnification* is $M = \pm 1$. The increment of $|x_2|$ resulting from the variation of the electron energy E characterizes the *dispersion* of the spectrometer, D. It has a dimension of length. For the parallel plate spectrometer in Fig. (12.5), $D = l$. The dispersion should be large to obtain small ΔE, i.e. good resolution for a given image slit size w_i.

The angular difference $|\alpha - \alpha_0|$ attributed to the increment of $|x_2|$ characterizes the focusing power of the spectrometer in the direction of the polar angle. Let us recall here that $|\alpha - \alpha_0| \leq \Delta\alpha$. The focusing power is significant when the increment of $|x_2|$ is small for large values of $\Delta\alpha$. Since $\Delta\alpha \ll 1$, good focusing can be obtained when the low power terms cancel in the Taylor expansion. With $n = 2$ in Eq. (12.10), only the first term is cancelled and the spectrometer is said to focus in first order.

The derivatives in the Taylor expansion depend on the geometric parameters

of the spectrometer. In general it follows that the number of derivatives which may be cancelled is equal to the number of adjustable geometric parameters. In the example given in Fig. (12.5) there are two such parameters, i.e. the deflection angle α_D and the distance between the planes of the object and entrance slit g. With a suitable choice ($\alpha_D = 60°$, $g = \sqrt{3}/6\ l$) it is possible to cancel the first two terms, i.e. the spectrometer focuses in second order ($n = 3$). In spectrometers where the object and the image slit coincide with the entrance and the exit slit, respectively, the distance g is fixed to zero. In this case only the parameter α_D is adjustable. Therefore, only one term may be cancelled and, consequently, the spectrometer focuses in first order only.

The polar aberration term P in Eq. (12.10) shows how much the first nonvanishing term in $\Delta\alpha$ shifts the position of the trajectory at the image slit. Hence, the (polar) focusing power is characterized by n and P.

In addition to the focusing with respect to the polar angle the spectrometer may have the capability to focus in azimuthal direction. Accordingly, these spectrometers are denoted as doubly focusing instruments. The toroidal, the cylindrical mirror spectrometer and the concentric hemispherical analyzer focus in the azimuthal direction in any order. This follows from the fact that the plates of these spectrometers are curved with respect to the azimuthal angle. Likewise, the spectrometers whose plates are flat with respect to that angle do not focus in the azimuthal direction. They are denoted as singly focusing instruments. In Eq. (12.10) the azimuthal aberration is accounted by A and m. It is noted here that for spectrometers without azimuthal focusing $m = 2$, while for those focusing in any order in the azimuthal direction, $A = 0$.

By varying the kinetic energy of the emitted electrons while E_0 is kept constant and counting the detected electrons, one gets the transmission function characteristic of the spectrometer. It usually has a triangular or trapezoidal form distorted by the angular aberrations. The energy resolution of the spectrometer ΔE is defined as the FWHM of the transmission function. The accurate determination of ΔE is rather complicated. Instead, the base width of the transmission function ΔE_B is calculated [89]

$$\frac{\Delta E_B}{E_0} = \frac{w_o + w_i}{D} + c_P(\Delta\alpha)^n + c_A(\Delta\beta)^m, \tag{12.11}$$

where the constants c_P and c_A are the polar and azimuthal aberration coefficients, respectively. It is usually a good approximation to take the energy resolution equal to the half of the base width, $\Delta E = \Delta E_B/2$ [89]. The important message of Eq. (12.11) is that the quantity which is determined by the geometry of the spectrometer is not the absolute but the relative energy resolution. This is generally true for energy dispersive electrostatic spectrometers.

There are some other important operational requirements of most analyzers, namely the fringe field plates. For reasons of clarity, they are not shown in Figs. (12.4) and (12.5). Obviously, it is not practical to construct analyzers

that are much larger in size than the distance between the slits. However, the electrons passing trough the analyzer must see only uniform fields to avoid severe aberrations. Therefore, the field of the analyzer must be terminated at each end to avoid field distortion in the aperture region. The termination can be realized by a series of electrodes (e.g. narrow plates for the parallel plate, ring shaped electrodes for the cylindrical mirror, etc.) whose potentials are set by dividing resistors to ensure a smooth transition between the analyzer electrode potentials. Another solution for the termination is the use of ceramic surfaces coated with resistor films.

However, fringe fields are produced by the slits too. The larger the ratio of the slit size to the distance of the analyzer electrodes, more strongly the electrons are deflected by fringe fields around the slits. When characterizing a spectrometer, it is important to quantitatively know this effect. Fringe field distortions of this kind can be significantly reduced by covering the slits with high transmission metal grids. Of course, fringe fields and electron scattering on the grids and the edges of the slits decrease the maximum value of the transmission.

Spectrometers for target Auger spectroscopy

Various aspects have to be considered when a choice is made between the various types of spectrometers. Favorable features of the spectrometers are high resolution, efficiency, and simplicity of design. High resolution is required when individual Auger lines are to be measured. Natural line width and separation of adjacent lines are of the order of 0.1 eV to 1 eV. Accordingly, resolutions $\Delta E/E$ of 10^{-4} to 10^{-3} are required using, e.g., 1000 eV electrons. In principle such resolutions may be realized by reduction of the spectrometer slits or by deceleration of the electrons. The latter method takes advantage of the fact that $\Delta E/E$ is usually constant so that the reduction of E decreases ΔE. The deceleration method is advantageous, since the loss in the spectrometer efficiency is usually lower than that originating from the reduction of the slit sizes. Furthermore, the deceleration method allows variation in ΔE during the measurements.

The simplicity of the spectrometer design is related to disturbance effects involved in the electron measurements. Significant experimental problems are produced by stray electrons reaching the detector and by spurious electric and magnetic fields. For instance, low energy electrons are significantly affected by the earth magnetic field. For high-resolution measurements it is required to reduce the earth magnetic field by a factor of about 100. This can be done by Helmholz compensation coils [13] or by Mu metal shielding vessel (see Fig.12.3) placed inside the scattering chambers [13,103].

At a given target size and desired luminosity, the resolution of an electrostatic spectrometer can be improved by increasing its size. Spurious electric fields and slit-edge effects can be significantly reduced in this way, too. Unfor-

tunately, longer electron trajectories make the arrangement more sensitive to remaining magnetic fields. A better magnetic shielding in a larger chamber, however, increases the cost of the apparatus significantly.

Similarly, spurious electric fields must be avoided. They are generally produced by electrons collected at insulating surfaces (e.g. contaminated by finger prints). Such fields are critical near the target region as they may produce energy shifts of the electrons of some eV. Spectrometers, which can be placed outside the target region, combined with gas-jet targets minimize such effects. Different temperature-dependent contact potentials of the materials used in the scattering chamber and the spectrometer shift the line positions. The best solution to avoid these effects is to coat all the metal surfaces with a slide of gold or graphite.

The most serious problem for electron spectroscopy in ion-atom collisions is stray electrons producing background signals. Electrons are similar to diffusing gas atoms in finding their way through tiny holes (Actually, they are worse since they tend to multiply—see the electron multiplier). Openings are always present in order that the spectrometer can be evacuated. Hence, considerable effort has to be made to prevent spurious electrons from reaching the detector. Experience shows that it is easier to control the spurious effects when instruments of simpler design are used.

A significant source of stray electrons is the backplate scattering. All the electrons from the target with energies larger then the actual pass energy of the spectrometer hit the negative voltage plate (see Fig. (12.5)). They are not only scattered but multiplied. The electric field of the analyzer accelerates these electrons in the direction of the base plate. Many of them may arrive at the detector producing background counts. To avoid this problem, one may use a grid instead of a solid backplate. The backplate can be coated by materials of low secondary emission (e.g., graphite). Collimators and a repulsive electric field can be used in front of the detector. The best solution, however, is the use of a double pass or tandem spectrometer (see e.g. Fig. (12.7)). In this case, the electron beam is analyzed by two stages of the spectrometer consecutively. Stray electrons produced by backplate scattering in the first analyzer will enter but not pass the second stage, since their energies and angles are different from those of the signal electrons. Tandem spectrometers have other advantages, too, relevant in high resolution spectroscopy. They provide more degrees of freedom to find the solution for high luminosity and high resolution at a specific target geometry.

Let us consider now the spectrometers most often used in high resolution Auger studies at the beamlines of accelerators.

Parallel plate The single focusing parallel plate spectrometer has been widely used in many fields in atomic collision physics including target Auger spectroscopy (see e.g., [23,24,51,75,103,104]). Its dispersion is sufficiently high to achieve good energy resolution. Focusing in first order as well as second order has been realized for this spectrometer. The first order focusing type

(with $\alpha_D = 90°$) has an object slit located at the entrance slit [93]. The parallel plate spectrometer that focuses in second order has separate object and entrance slits and $\alpha_D = 60°$ [94]. The luminosity of the parallel plate spectrometer is small for point-like sources but rather good for extended sources. Fringe field distortions are relatively small. Source and detector positions well outside the spectrometer are advantageous. Compact tandem versions are also widely used (see e.g. [105]). Deceleration or acceleration lenses can be conveniently fitted to the spectrometer. The main advantages are the simplicity in construction, compact arrangement, and small size. This makes it easily applicable in angular distribution measurements.

In order to illustrate the resolving power of a parallel plate spectrometer ($\alpha_D = 90°$) used with deceleration, a few diagram lines of the Ar L-Auger spectrum are shown in Fig. 12.6 [106]. The data were taken by electron impact on a gas-jet target. The Auger electrons were decelerated down to 3 eV pass energy. The half width of the spectrometer function was measured to be 90 ± 15 meV.

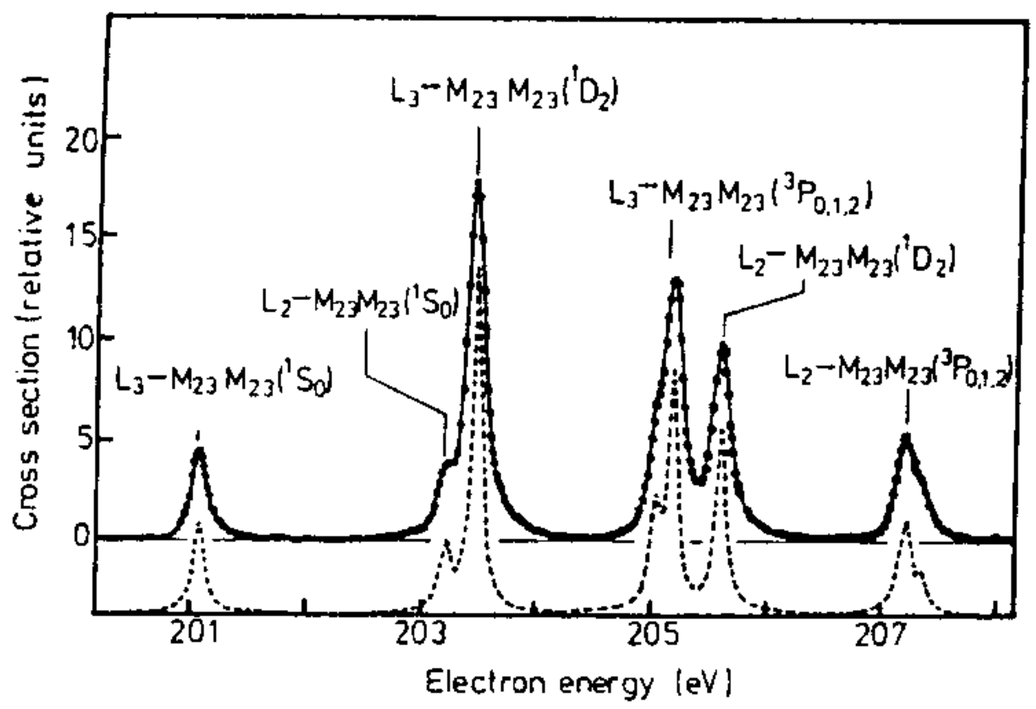

FIGURE 12.6 Part of the Ar L-MM Auger spectrum excited by 2.5 keV electrons. Full curve: result of computer fit; broken curve: deconvoluted spectrum. Reprinted from D. Ridder, J. Dieringer and N. Stolterfoht, "Fine-structure splitting of the L_2 $^3P_{0,1,2}$ Auger lines in argon" [106], with kind permission of IOP Publishing Limited.

From Fig. 12.6, it is clearly seen that the finite energy resolution broadens the natural line widths only slightly. The fine structure splitting of the multiplets can be studied quantitatively. One should note, however, that it was necessary to use an electron beam current of 1 mA to achieve good statistics.

Cylindrical plate The cylindrical plate spectrometer is a single focusing instrument with a first order focus at $\alpha_D = 127°$. It has been used in atomic collision experiments since the early sixties (see the review of Rudd and Macek [13] and references therein). Its main characteristics are similar to the parallel plate but the construction is a bit more complicated, the size is larger, the luminosity is slightly smaller, and fringe field distortions are stronger.

Concentric hemispherical analyzer (CHA) Studies performed by means of CHA and its sector versions have been reported by many authors in studies concerning target Auger spectroscopy (see e.g., refs. [26,48,52,107]). With $\alpha_D = 180°$, it is doubly focusing with first-order focus in the polar direction, and any-order focus in the azimuthal direction. In the sector versions of CHA ($\alpha_D < 180°$,), second order focus can also be obtained. For extended sources, it is possible to achieve high resolution and high luminosity simultaneously. The construction is rather complicated. Commercial versions are also available. Source and detector positions are outside the analyzer, therefore it is well suited to the use of acceleration or deceleration lenses and for angular distribution measurements.

Cylindrical mirror analyzer (CMA) The solid angle of the spectrometer increases considerably when a larger azimuthal angular range is accepted. This is realized by the cylindrical mirror analyzer [108]. Moreover, CMA has a remarkably large polar acceptance angle, too. Among the frequently used spectrometers CMA has the largest value of brightness at a given resolution. Design and construction is relatively simple. A special feature of CMA is that it has several focal conditions. It can focus e.g., from point to point and from point to ring in both first and second order. In the most often used point-to-point double focusing arrangement, $\alpha_D = 84°$. Because of its large solid angle the spectrometer is widely used in the field of electron spectroscopy for chemical analysis (ESCA) [37].

The application of CMA in collision experiments is not simple. The target region is localized inside the inner cylinder. It is difficult to use high density gas targets there since the diffusing gas may not readily be pumped away. Preacceleration or deceleration is difficult to perform. If the ion beam is directed along the axis of the spectrometer, providing the largest solid angle, the electron observation angle relative to the incident beam is fixed to $\alpha_0 = 42°$ and cannot be varied. Part of the difficulties were removed by Toburen [109] by using a CMA constructed from half cylinders and locating it relatively far away from the target region. Woods *et al.* [53] rotated the axis of a CMA by 132° with respect to the ion beam axis so that electrons ejected from 90° to 174° in the laboratory frame were analyzed. In this way they achieved a high luminosity at backward angles. This is especially advantageous when the total Auger production is to be measured, since the continuous electron background is relatively small in this angular range.

New approaches were made by Varga *et al.* [110] and Kövér *et al.* [111,112]. Varga *et al.* [110] constructed a distorted field version of CMA. By calculating the electron trajectories in different systems, they found that a box-type termination of the cylinders (see Fig. (12.7a) provides good focusing properties and energy resolution with object and image focal points outside the box. In the application, Kövér *et al.* [111,112] directed the ion beam through the target region of the distorted-field tandem CMA on such a way, that the ion beam could pass one of the entrance slits for the electrons. This arrangement

was similar to that of Woods *et al.* [53] but the aim was different. Evidently, it was necessary to make a hole on the outer cylinder of the CMA to allow the beam to enter the Faraday cup. In such a way the different electron trajectories in the CMA belong to different polar emission angles relative to the beam direction. Hence, within a limited region an angular distribution measurement can be performed *by rotating only the electron detector* which is mounted on an angle defining cylinder. Typically, gas-jet targets have been used in the experiments. The schematic view of the spectrometer and its possible positions relative to the beam are shown in Fig (12.7).

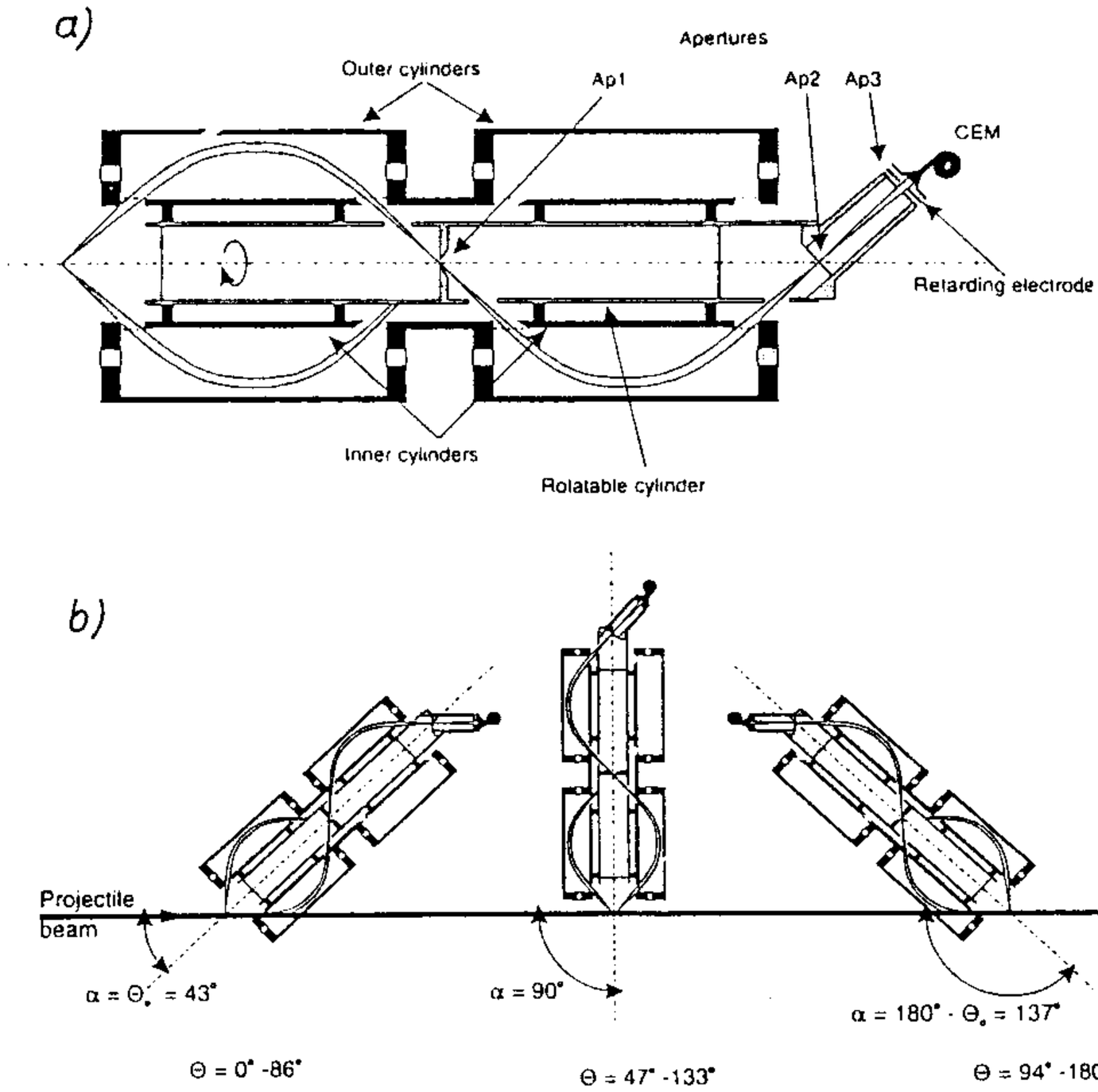

FIGURE 12.7 Schematic view of a distorted field tandem CMA spectrometer (a) and its possible positions for angular distribution measurements (b). Reprinted from Á. Kövér, D. Varga, I. Cserny, E. Szmola, Gy. Mórik, L. Gulyás and K. Tokési, "A distorted field cylindrical mirror electron analyzer, 2. Performances and application for studying ion - atom collisions" [112], with kind permission of Elsevier Science - NL, Sara Burgerhartstraat 25, 1055 KV Amsterdam, The Netherlands.

The arrangement in Fig. (12.7) has many advantages. It is possible, e.g., to measure angular distributions in fine steps, even around 0° and 180°. There are no changes in the target region when the observation angle is changed. Large solid angle and high resolution of the original CMA has been retained. The main disadvantage is that there is no simple way to apply a pre-deceleration lens. Hence, the energy resolution is limited by the (variable) slit sizes of the spectrometer.

Also, when performing angular distribution measurement using the spectrometer shown in Fig (12.7), for varying the observation angle one still needs to change the detector position. An entirely different approach, measuring the total angular distribution simultaneously, was made by Varga *et al.* [54,57,113,114]. They constructed a multidetector instrument which accepts the full range of the polar angle Θ relative to the beam direction. The spectrometer is divided into several angular sectors, each of which is equipped with a channeltron detector allowing for the individual registration of the electrons. Hence, electrons may be measured simultaneously under 13 polar angles relative to the beam direction including 0° and 180°. The schematic diagram and a perspective view of their spectrometer is displayed in Fig (12.8).

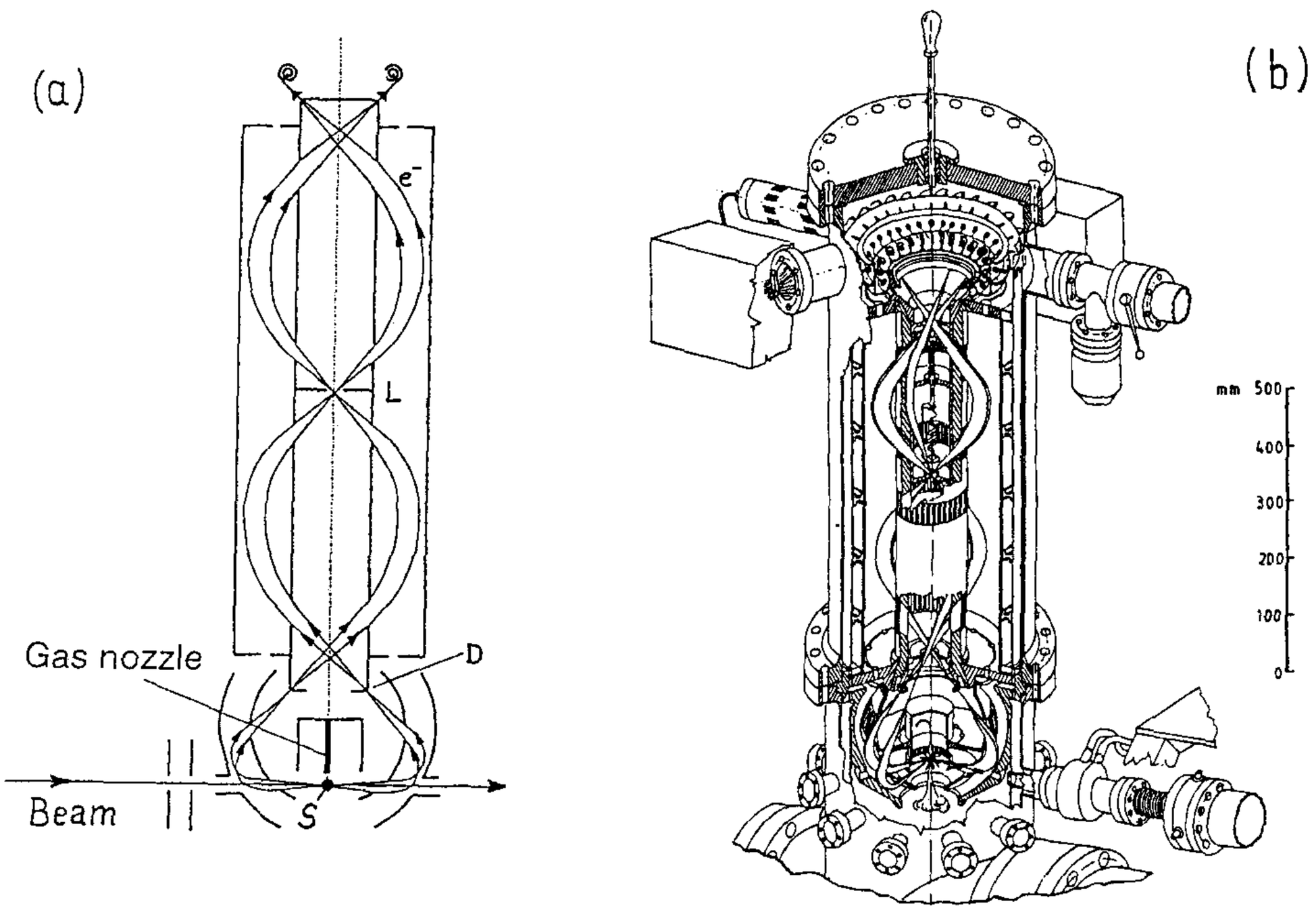

FIGURE 12.8 Schematic cross section (a) and persective view (b) of the spherical + double cylindrical mirror spectrometer for simultaneous angular distribution measurements. Part (b) is reprinted from D. Varga, I. Kádár, S. Ricz, J. Végh, Á. Kövér, B. Sulik and D. Berényi, "A spherical mirror – double cylindrical mirror electron spectrometer for simultaneous energy and angular distribution measurements" [114], with kind permission of Elsevier Science - NL, Sara Burgerhartstraat 25, 1055 KV Amsterdam, The Netherlands.

The spectrometer consists of a spherical mirror and a double-pass CMA. The spherical mirror collects all electrons ejected from the source S in the azimuthal plane and focuses them into a ring D at the entrance of the first CMA. The double-pass CMA focuses ring to ring. On the image ring, 13 channeltron

detectors are located in 15° angular steps from 0° to 180°. Between the two CMA stages there is a focal point at L. The spherical mirror has large angular focusing power and a fairly poor (10%) energy resolution. Its role is only to project the source to the focal ring D with proper angular conditions for the CMAs. Resolution and solid angle are determined by the double pass CMA. The source - detector distance is 795 mm. The carefully collimated ion beam with a diameter of 2.5 mm crosses the spherical mirror. Its deflection by the electric field is negligible for ion impact energies larger than 100 keV. A gas-jet target is located above the source point S and directed downwards. The energy resolution can be improved by a spherical ring deceleration lens located around the target. It is constructed with finite-size holes at all the angular channels. No grids are used in the target region. CMA slit sizes can be changed from outside the vacuum chamber. In this way, the relative energy resolution can be varied between 0.05 % and 0.6 % without deceleration. At 0.6 % relative resolution, the solid angle is $\approx$ 0.15 % per angular channel. We would like to mention here that the spectrum shown in Fig. 12.6 has also been measured by means of the above triple-pass spectrometer with the same instrumental resolution. However, in contrast to the 1 mA, in that case the electron beam current needed to arrive at good statistics in the single angular channels within a few hours was below 1 μA. This difference shows that a large CMA has excellent luminosity.

A few experimental results obtained with the help of the above two spectrometers are presented in the forthcoming sections.

It is recalled here that both CMA and CHA are special cases of the toroidal spectrometer (see Fig. 12.4) [96]. For toroidal spectrometers other than CMA or CHA, however, both theory and design is rather complicated. First applications in e-2e measurements were reported only recently [97–99].

Other spectrometers

There are instruments using methods other than electrostatic field deflection for the energy analysis of the electrons. For instance, instead of electric fields one may apply magnetic fields to deflect the electrons. The magnetic spectrometers are often chosen to analyze high-energy electrons such as those produced by nuclear beta decay [115]. In atomic collision experiments, magnetic spectrometers are utilized when electrons above about 20 keV are to be measured.

Moreover, there are non-dispersive instruments applying the retarding field method (see e.g., ref. [116]). Generally, these spectrometers have huge solid angles. However, the measured curve has to be differentiated to achieve the corresponding electron spectrum. The differentiation creates significant statistical errors so that the advantage of the large solid angle is partially cancelled. A method to achieve dispersion with this spectrometer is the focusing of the near-zero energy electrons which barely have passed the retarding field thresh-

old onto the detector [116]. Unfortunately, in this case it is difficult to avoid problems produced by background electrons.

A further dispersive instrument is the time-of-flight spectrometer [117]. The time-of-flight method, however, requires pulsed incident beams or electron-ion coincidence measurements. The spectrometer itself is relatively simple. It consists essentially of a drift tube. The instrumental effort has to go into the electronic part, which must be able to handle pulses in the subnanosecond region. Since electrons are relatively fast, only energies below about 200 eV have been treated by the time-of-flight method [117]. Pre-deceleration may extend this energy range. The solid angle of the time-of-flight spectrometer is much larger than the electrostatic analyzers. This makes it well suited for coincidence measurements, where high resolution electrostatic analyzers provide low count rates.

12.3.4 Electron detectors

After passing the spectrometer, the energy-analyzed electrons are detected by electron multipliers. Three main type of multipliers are most often used for detecting electrons in the few eV - few keV kinetic energy range.

The first is the traditional, high sensitivity multiplier constructed from discrete dynodes. It provides a high efficiency ($\eta = 0.8 - 0.98$) which is rather stable in a wide energy range. The accepted count rate is a few hundreds of kHz, rather large. An advantage of it is the large sensitive area, while the related disadvantage is its large size. Unfortunately, this detector must be kept continuously in high vacuum to avoid surface damages and efficiency degradation.

In general, the channel electron multiplier (channeltron) has a lower efficiency ($\eta = 0.3 - 0.8$) and a limited count rate (80-100 kHz). Depending on the manufacturer and the technology, their efficiency may vary with the electron energy in different ways. It is usually constant or only slightly changing above 100 eV. It can be kept at open air for long times without significant degradation but not without the change of efficiency. The small size makes it attractive in many applications.

The main deficiency of the channeltrons is not always recognized. It is the dependence of the efficiency on the place of the electron impact within the sensitive area. The less sensitive part is the center, where the electrons fall deep into the tube and the multiplication factor drops by a factor of 2-8. It may happen that a sharp focusing into the center of the detector decreases the count rate by a factor of five [118].

Channel plate (microchannel plate) is also widely used for electron detection. Its efficiency is usually more stable and less energy dependent than that of channeltrons. However, they are not advised to keep in open air for a longer time. Channel plates are able to accept as high (or sometimes higher) count rates as the discrete-dynode multipliers. Their main drawback is the relatively

large dark count rate. In some energy-dispersive spectrometers, channel plates are used as position-sensitive detectors located in the focal plane of the spectrometer, in order to take a wider region of the energy spectrum in one step. They are also used for the simultaneous angular distribution measurement in toroidal spectrometers. Since they have extremely good timing properties, channel plates are the most advanced detectors in time of flight spectrometers and in any coincidence measurements.

We would like to emphasize that a signal of a detector can only be considered as a count if it passes the discriminator. All kinds of multipliers are very sensitive on the proper setting of the high voltage. The optimization of the signal-to-noise ratio and the right setting of the discrimination level are also essential to utilize the potential efficiency of the detector. If all these conditions are fulfilled, the determination of the detector efficiency is still a hard task. Different methods (independent current measurement, reference proportional counter, etc.) are referred by Rudd *et al.* [27]. Since the efficiency of multipliers of any art is usually not very stable in time, only absolute calibration is advised for absolute measurements.

12.3.5 Data acquisition and spectrometer control

Electrostatic electron spectrometers, as well as acceleration or deceleration lenses, need well-calibrated, low-noise, accurate high voltage power supplies. In high-resolution Auger studies, the necessary overall accuracy is typically better then 10^{-4}. The setting of the high voltage power supplies is usually controlled by a computer via digital/analog converters. The spectra are taken successively, collecting the same amount of charge by the beam-Faraday cup for every step. Electron signals provided by the discriminator(s) are also counted by the computer. The spectra are usually taken in several consecutive runs to ensure the possibility for reproducibility and reliability checks to be performed later.

The above setup and procedure is generally well known. The reliability test of the measured spectra is usually performed by visual comparison of the different scans. If, however, the cross section of the studied process, i.e., the number of counts in one scan, is small, less approximate methods should be applied. Such mathematical procedure for post-measurement reliably test has been developed and used by Végh *et al.* [85]. Finally, we would like to call attention to the fact that slow power supplies for the varied spectrometer voltages and slow current integrators cannot be used in electron spectroscopy. For obvious reasons, these electronic elements have to be much faster than the possible minimum time interval for taking one energy point of the spectrum.

It is noted here that although accurate power supplies are essential in high-resolution studies, the best way to calibrate the energy scale of the full experimental setup is to measure reference Auger lines with accurately known energies.

12.3.6 Collision kinematics

After the collision, both projectile and recoil ions are moving. Since the Auger process is slow compared to the collision time, the Auger electron always originates from a moving emitter. Such kinematic effects may destroy the available energy and angular resolution. A detailed analysis of the kinematic effects has been performed Rudd and Macek [13]. More recent work is treated by Stolterfoht [9] (see also the references therein) for both target and projectile Auger spectroscopy. Here we recall only the results most relevant to target Auger spectroscopy.

Let us assume that the Rutherford formula is a good approximation for treating the energy transfer between the nuclei of the two colliding atoms. Then, for not too small impact energies, the energy transfer to the target nucleus *at a fixed impact parameter* is inversely proportional to the projectile impact energy, $T_2 = const/T_1$ [25]. Sometimes, this relation is quoted as *kinematic paradoxon* [9]. Most of the atomic collision mechanisms can be associated with a certain impact parameter region. For K-shell ionization, e.g., the average impact parameter is of the order of the K-shell radius (and it may increase slightly with increasing impact velocities).

Kinetic energy transfer to the target atom yields line broadening. As a rough estimation in energetic ion-atom collisions, the velocity distribution of the recoil target atoms can be considered as being isotropic in a plane perpendicular to the beam direction. Accordingly, line broadening originating from the Doppler effect shows a maximum at 90° observation angle and a minimum at 0° and 180°. Heavy ion impact at relatively low energies may completely destroy the resolution and wash out any structures from the Auger spectrum.

Fortunately, due to the kinematic paradoxon, Doppler broadening can be significantly reduced by increasing the impact energy of the heavy ions. The effect is illustrated in Fig.(12.9), comparing Ne K-Auger spectra produced by 500 keV Ne^+ [103] and 30 MeV O^{5+} [119] bombardment. Although the instrumental resolutions are nearly equal for the two spectra, the 30 MeV O^{5+} spectrum exhibits line structures that are totally washed out in the 500 keV Ne^+ spectrum. This shows that high-energy accelerators are very useful for the measurement of electrons from recoil target atoms. Indeed, high resolution Auger spectroscopy studies have been performed using either light ions or a few MeV/u heavy ions.

For heavy ions of a few MeV/u or higher energy range, however, nuclear reaction channels may also be open. Among other problems, nuclear reactions can significantly contribute to the background of the atomic physics measurement. Neutrons and high-energy γ photons can easily provide stray electrons inside or in front of the electron detectors. For strongly collimated beams the majority of the nuclear background signal originates from the first beam-collimator aperture. Often, a negative correlation exists between the first-slit current and the Faraday current. Obviously, such a negative correlation may

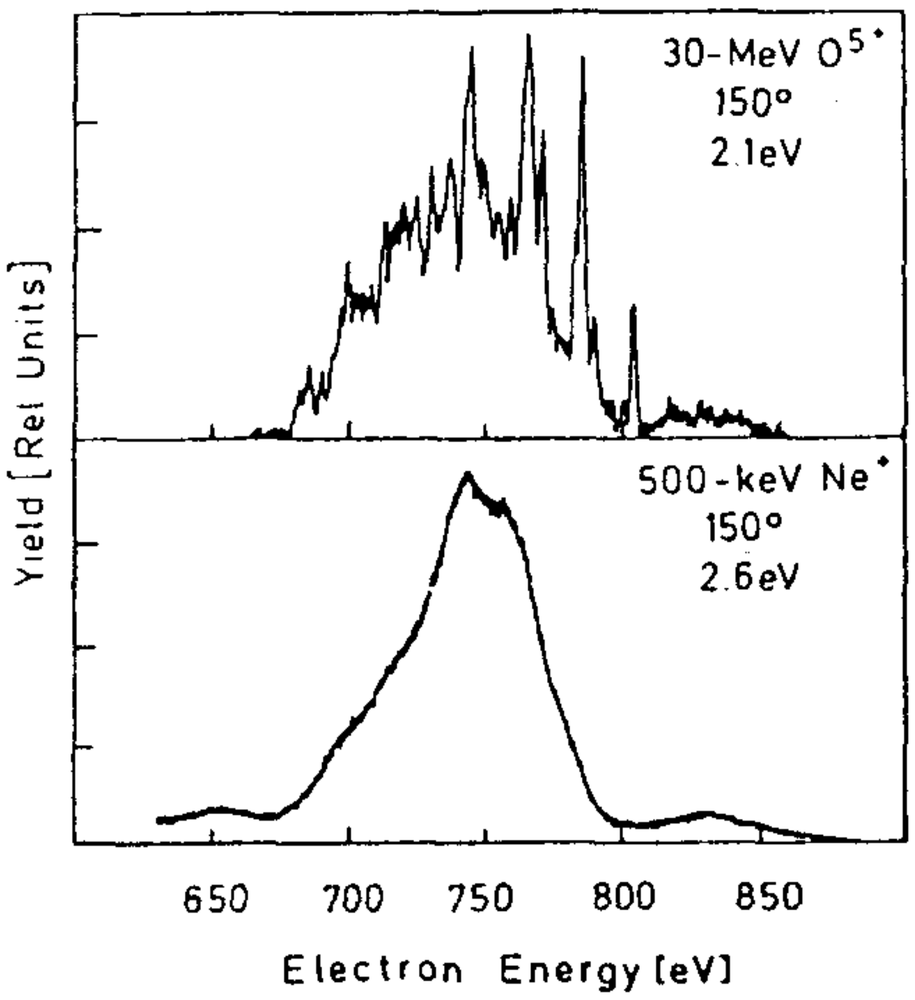

FIGURE 12.9 Ne K-Auger spectra excited by 30 MeV O^{5+} impact [119] and 500 keV Ne^{+} [103] impact. The observation angle is 150° and the energy resolution (FWHM) is indicated in the figure. Reprinted with permission from *Phys. Rev. A* **12** (1975) 1313.

yield much larger errors in the spectrum than a more intensive background component which is proportional to the collected charge. Therefore the first collimator aperture must be located as far away as possible from the scattering chamber. At pulsed beam accelerators, coincidence methods can also be utilized to reduce the nuclear component of the background [85].

12.4 EXPERIMENTAL STUDIES

In this section, a few experimental studies are selected to illustrate the potentials of the methods and provide insight into the tendencies in the field. Three topics are considered.

12.4.1 Multiple ionization

The possibility to remove several electrons in a single collision and to reduce the kinematic broadening effects opened the field of high-resolution Auger spectroscopy of systems with high degree of multiple ionization. The effect of heavier projectile impact is demonstrated in Fig (12.10) [50] where various Ne K-Auger spectra are compared [50,75,119,120]. It is well known in the field of Auger spectroscopy that the mean energy of the satellite lines decreases as the number of L-shell vacancies increases. Therefore, from the spectra in Fig 12.10 it is concluded that the degree of outer-shell vacancy production increases strongly with increasing nuclear charge of the projectile. Moreover, it is seen that for the lightest and heaviest projectiles the spectrum consists

of only a limited number of lines. These lines belong to one or two vacancy states.

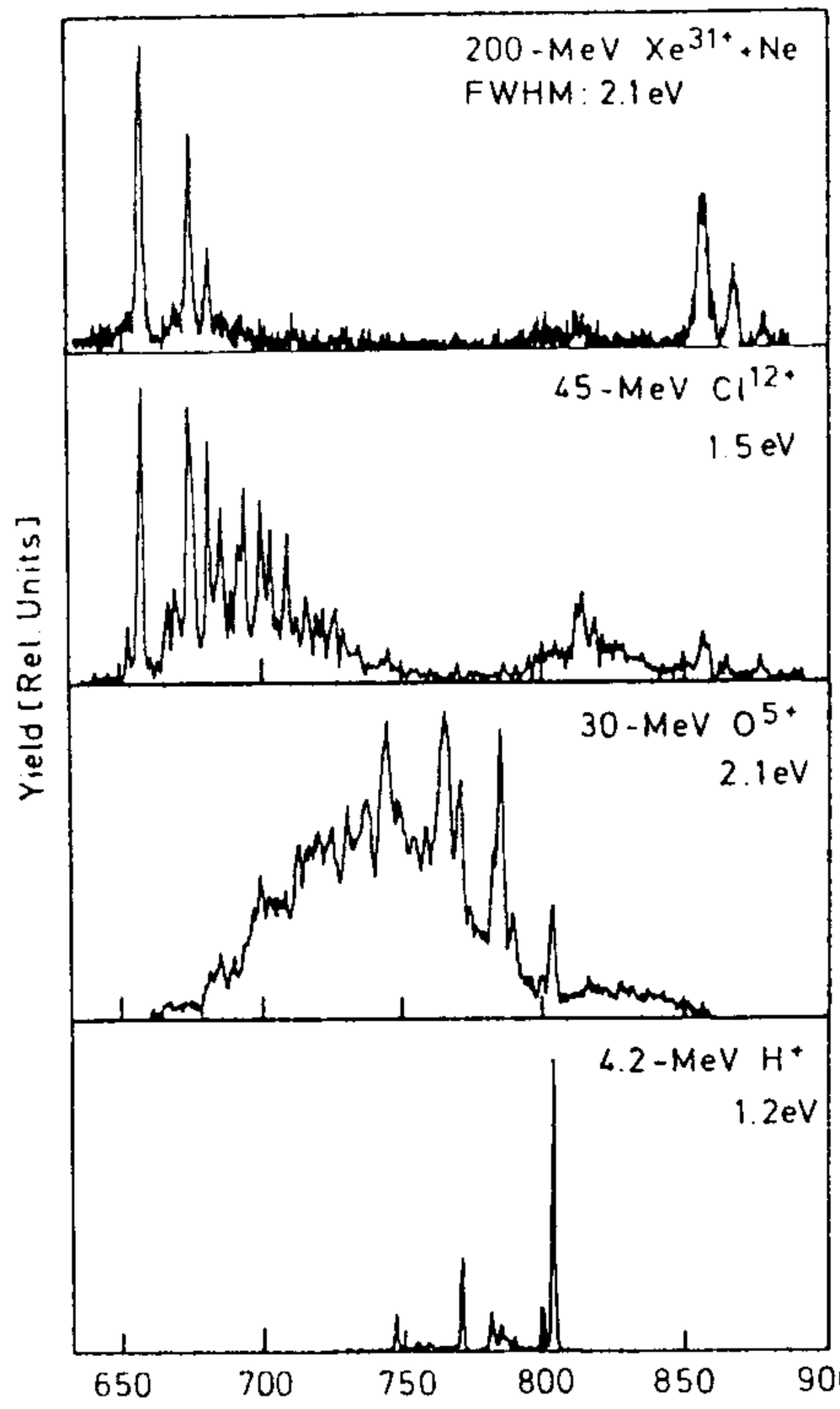

FIGURE 12.10 Comparison of Ne K-Auger spectra produced by 4.2 MeV H^+ [75], 30 MeV O^{5+} [119], 45 MeV Cl^{12+} [120] and 200 MeV Xe^{31+} [50] impact. Reprinted from N. Stolterfoht, D. Schneider, R. Mann and F. Folkmann, "Auger emission for highly ionized neon produced in 200 MeV Xe^{31+} + Ne collisions" [50], with kind permission of IOP Publishing Limited.

Several experimental studies have been devoted to determining the degree of multiple ionization of the Ne L-shell by performing high-resolution Auger electron measurements (see e.g. refs. [9,26,51,54,56,58]). In those experiments, a large variety of heavy ions was used. The analysis was based on the independent particle model (IPM) for multiple ionization. Within the framework of IPM, the vacancy population distribution P_n on the L-shell is binomial [121,122]

$$P_n = \binom{8}{n} p_L^n \, (1 - p_L)^{8-n},$$

where the parameter p_L is the average one-electron ionization probability for

the L-shell associated with K-shell ionization. Analogously, a double binomial distribution with two parameters can be used, assuming that the ionization probabilities are different for the 2s and 2p subshells. Within this framework, the determination of two or three members of the distribution is sufficient to derive a p_L value (or p_{2s} , p_{2p} values). Only a few lines in the Auger spectrum, belonging to two or three initial vacancy states, must be identified. Then, with the help of calculated branching ratios (see Eq. (12.4)), the relative populations of two or three initial vacancy states and the corresponding p_L value can be extracted. With this method, a linear connection between the centroid energy of the Ne K-LL Auger group and the average number of L-shell vacancies was established and verified experimentally [51,54].

Obviously, the above method is strongly model-dependent. The reliability of the derived probabilities depends on the applicability of IPM for the given collision system and the quality of the branching ratio calculations. A model-independent experimental determination of the total $2s - 2p$ vacancy distribution can be performed by identifying the majority of the lines in the Auger spectrum. For the neon target, many satellite Auger lines have been observed and identified by Matthews *et al.* [48] in H^+, He^+, and 30 MeV/u O^{5+} + Ne collisions.

As is shown in Fig. (12.10), different degrees of multiple ionization of the same target species can be achieved by varying the charge state of heavy projectiles in fast collisions. If the resolution is sufficiently high, and the degree of multiple ionization is varied in fine steps, a large portion of satellite lines associated with different initial vacancy states can be identified from the interrelated spectra. Such a systematic study was performed by Kádár *et al.* [56,57]. In those experiments, neon gas target was bombarded by 5.5 MeV/u H^+, N^{2+}, N^{7+}, Ne^{3+}, Ne^{10+}, Ar^{6+}, and Ar^{16+} ions at the beamlines of proton and heavy ion cyclotrons. The spectra were collected by the three-stage multidetector spectrometer displayed in Fig. (12.8) with deceleration at a constant 175 eV pass energy. The resolution was 1.05 eV for the 804.5 eV K-$L_{23}L_{32}$ diagram line of neon. Characteristic energy regions of the K-Auger spectra measured in Ar^{16+} -Ne and Ne^{3+} -Ne collisions are shown in Fig. (12.11).

In the line identification procedure calculated Auger transition energies and intensity ratios, experimentally determined target and projectile Auger spectroscopy data for F-, O-, Li-, and Be-like states, and optical spectroscopy data were used as references. Line-groups that changed their intensities together, when going from one projectile to another, were selected and analyzed separately before starting the next iteration of fitting and identification. As a result of this long procedure, 104 lines were identified from the observed 152 [57]. The intensity of the identified lines gives 80-85% of that of the total K-LL spectrum. All the non-identified lines were ordered to a given number of the L-shell vacancies. In such a way, full 2s-2p subshell vacancy distributions have been determined for Ne^{3+}, Ne^{10+},and Ar^{6+} projectiles. The distributions are

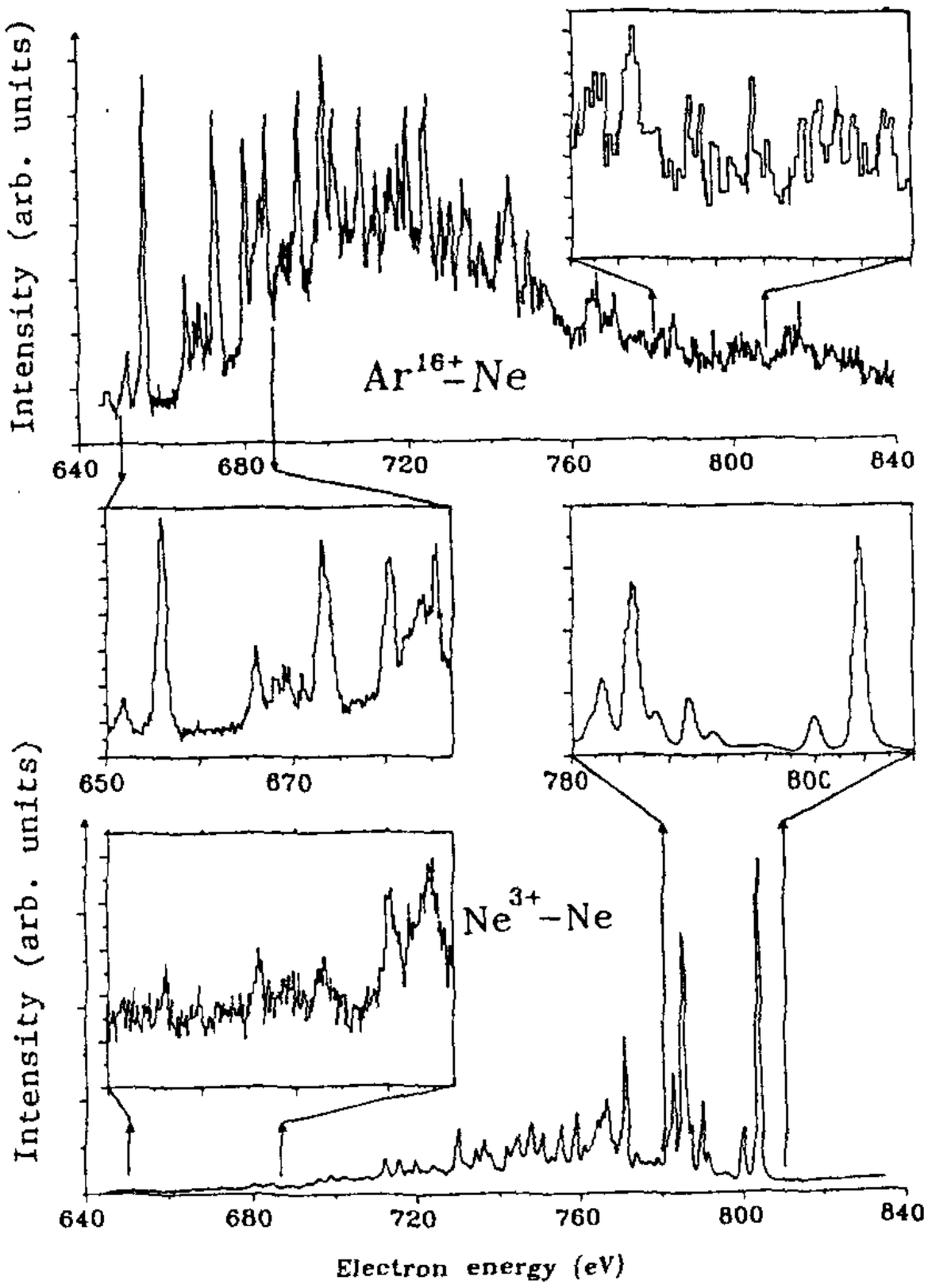

FIGURE 12.11 Selected characteristic energy regions of the K-Auger spectra measured in 5.5 MeV/u Ar^{16+} -Ne and Ne^{3+} -Ne collisions. *From* [57].

presented in (Fig (12.12)). A two-parameter binomial distribution (shadowed bars) has been fitted to the experimental data (black bars). The typical value of the relative statistical error of the experimental data is 5 % (*not shown* here).

A close inspection of Fig. 12.12 shows that the fitting is rather good for $Ne^{10+}$and Ar^{6+} but out of the statistical error limits for Ne^{3+}. The applicability of the independent particle model has not been strongly confirmed but no systematic deviations have been found from its predictions. The empty bars display the results of an independent calculation, performed by using a non-perturbative geometric binary encounter model of *Sulik et al. [58,123]. In* general the agreement between experiment and the independent theory is not much worst than between the experimental data and the fitted distributions.

For other projectiles listed above, only parts of the spectra were measured with good statistics. However, they provide sufficient information to extract subshell ionization probabilities within the IPM framework [58]. The data are displayed in Fig. 12.13, as a function of a scaling variable emerging from the

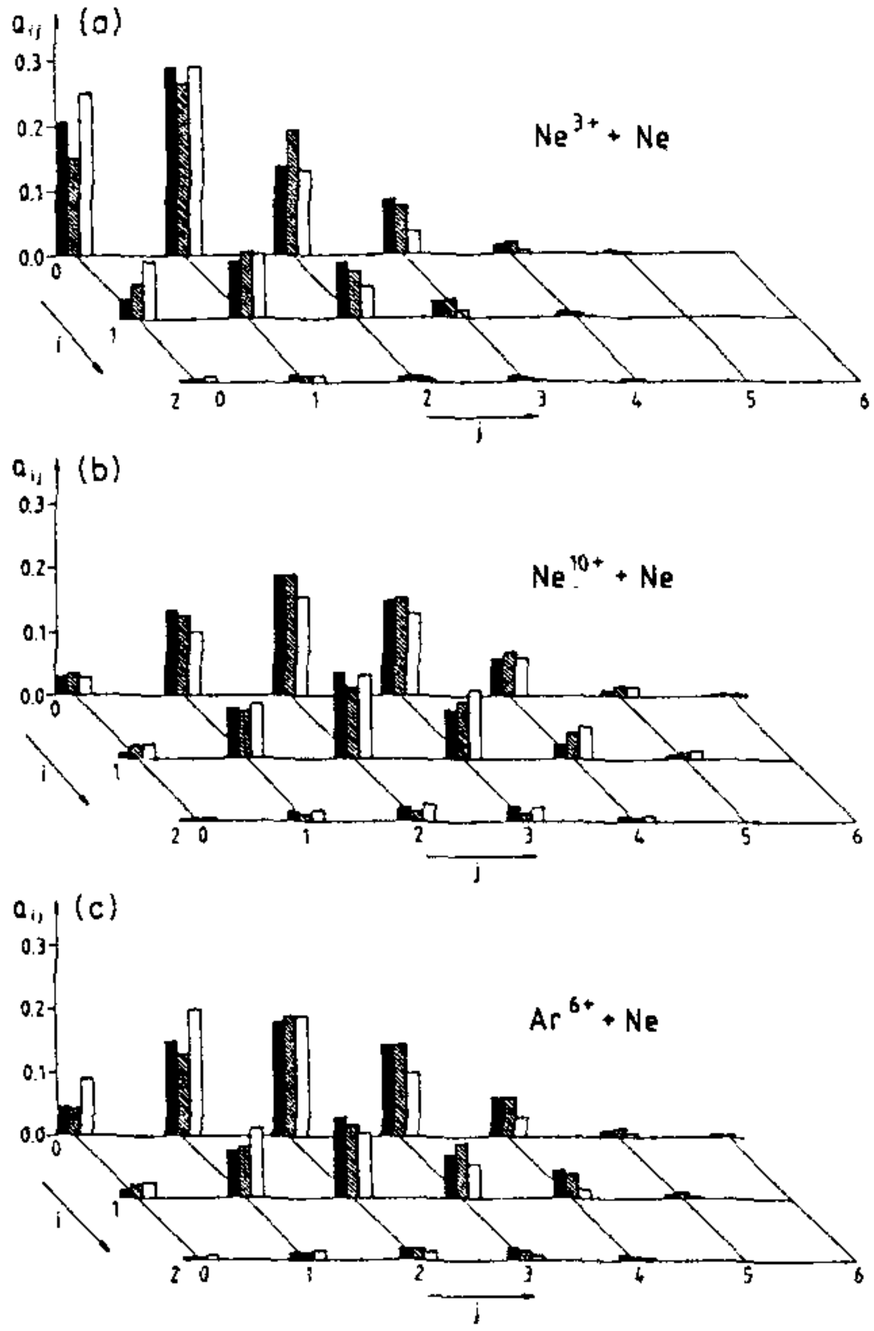

FIGURE 12.12 Experimentally determined vacancy configuration distributions (black bars) compared to the the double binomial distribution fitted to the experimental data (shadowed bars) and to the theory [58] (empty bars). Here i and j are the number of $2s$ and $2p$ vacancies, respectively. From [57].

theory [58,123]. In the present case, the scaling variable is proportional to the effective charge of the projectile. It is clearly seen that both the scaling properties and the absolute values are well-reproduced by the binary encounter model.

12.4.2 Angular distribution studies

Nonstatistical population of the magnetic substates in ion-atom collisions may happen by excitation to a $j > 1/2$ subshell or by creating a vacancy in it [16]. The latter can be performed by ionization, excitation or electron capture. For studying the collision mechanism and the fine details of the atomic/ionic structure, it is useful to start with the simplest systems. *Considering single* excitation followed by autoionization, the simplest target is Li. It has uniquely s electrons in the ground state $1s^2 2s\ ^2$S. Moreover, a *single* $1s - 2p$ excitation provides excited states that can decay by Auger process.

The angular distribution of the $1s2s2p\ ^2$P Auger lines of Li excited by H^+ and He^+ impact was studied by Ziem *et al.* [59]. Spectra are taken at different

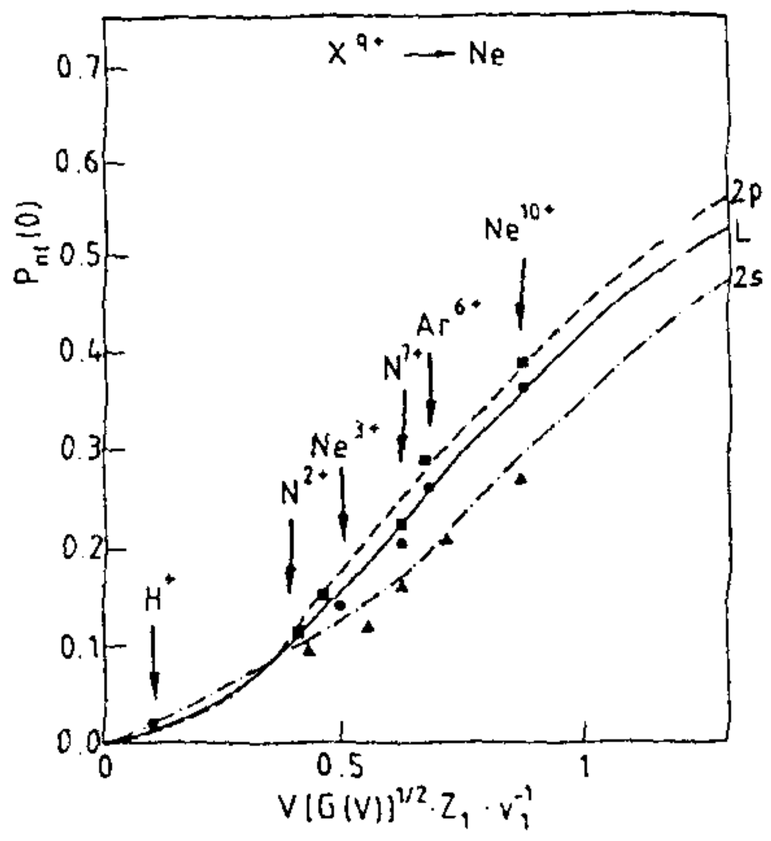

FIGURE 12.13 Experimental and theoretical ionization probabilities for Ne L-subshells produced by the impact of 5.5 MeV/u ions. Reprinted from B. Sulik, I. Kádár, S. Ricz, D. Varga, J. Végh, G. Hock and D. Berényi, "A *simple theoretical approach to multiple* ionization and its application for 5.1 and 5.5 MeV/u X^{9+} - Ne collisions" [58], with kind permission of Elsevier Science - NL, Sara Burgerhartstraat 25, 1055 KV Amsterdam, The Netherlands.

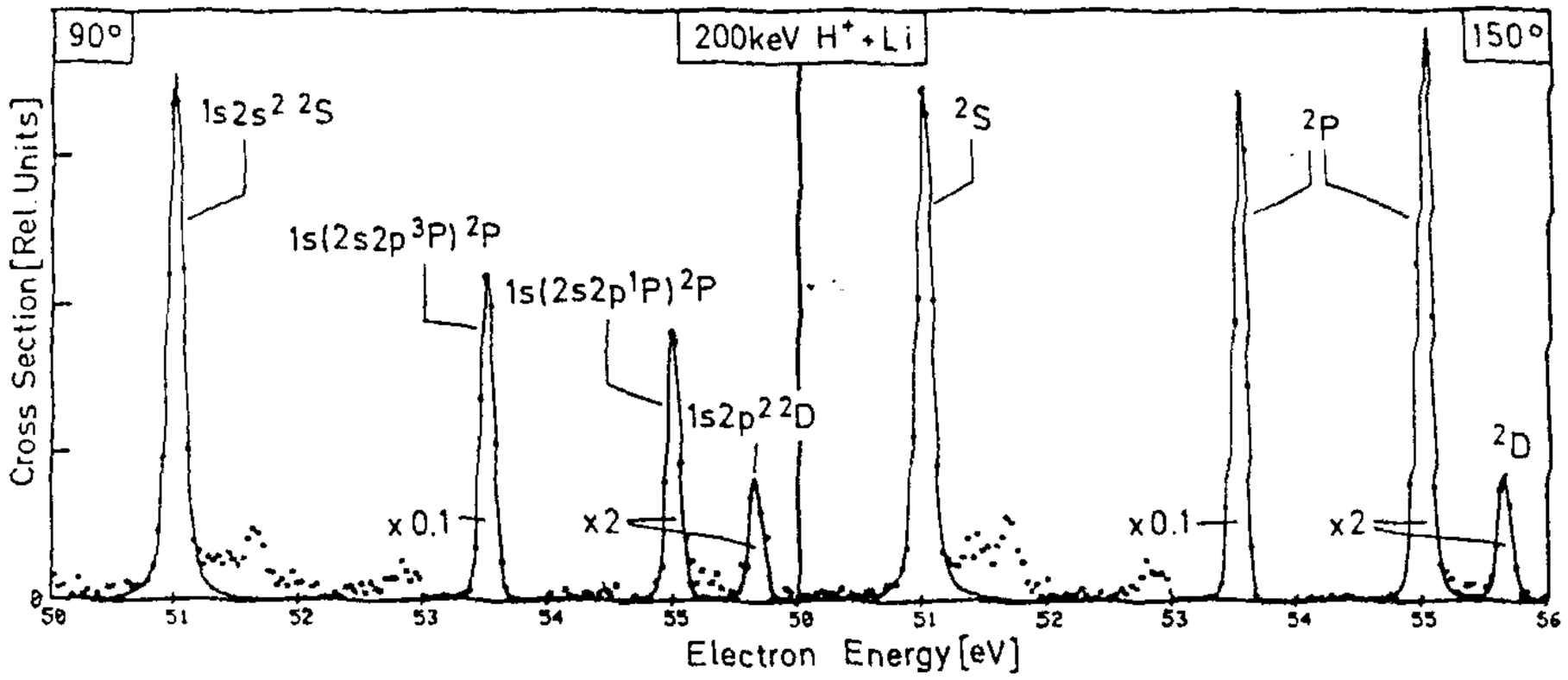

FIGURE 12.14 Lithium autoionization spectra measured at different angles by *200 keV* H+ impact. The full curves result from least-square fit of spectrometer functions to the data. Reprinted with permission from [59].

polar angles relative to the beam direction as displayed in *Fig. 12.14*.

The $1s2s^2\ ^2S$ line is isotropic. Therefore it can be used for normalization. Then, the two members of the $1s2s2p\ ^2P$ *doublet show definite anisotropy.* Moreover, their angular dependence is different. For these lines, Eq. (12.7) becomes very simple. There is only one term in the sum ($k = 2$), and $\alpha_2 = 1$

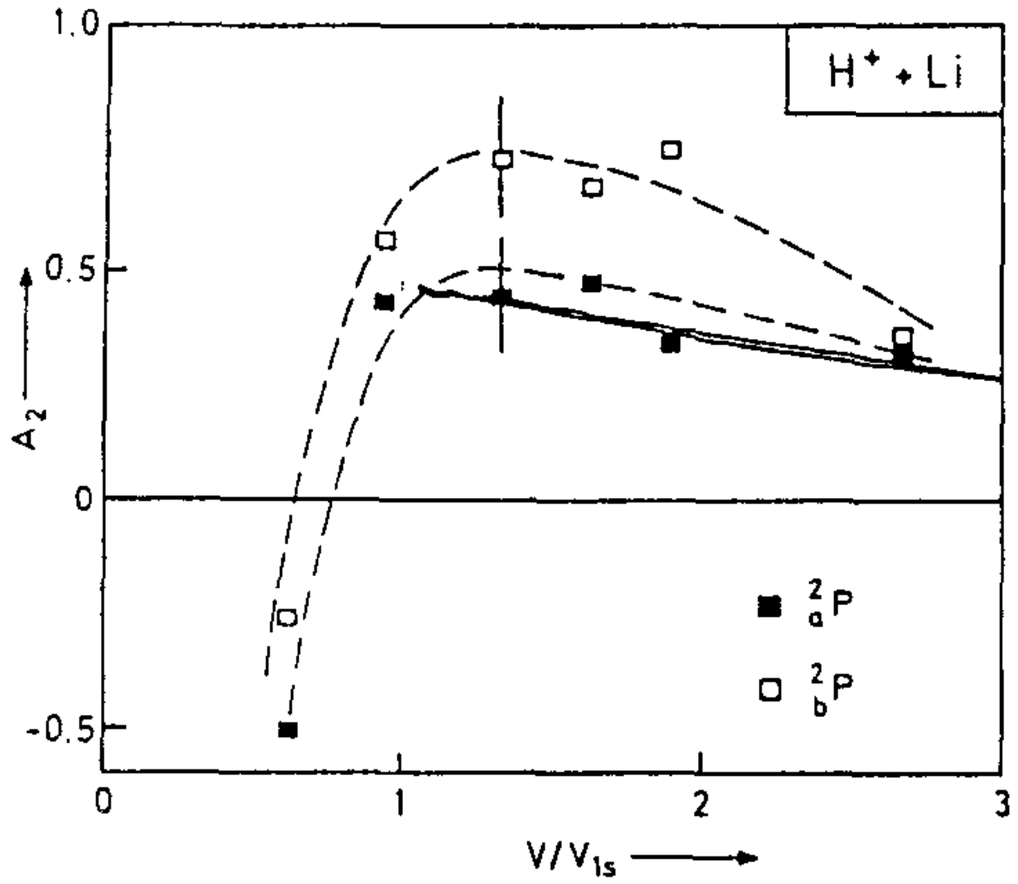

FIGURE 12.15 Alignment parameter A_{20} as a function of the projectile velocity v in units of v_{1s}. Data points are given for the ^2P_a (full symbols) and ^2P_b (open symbols) terms. The full lines are PWBA results multiplied by 0.3. The dashed curves are plotted to guide the eye. Reprinted with permission from [59].

(see e.g., ref. [16]).

$$I(\Theta) = \frac{I_0}{4\pi}\left(1 + A_{20}P_2(\cos\Theta)\right) \tag{12.12}$$

Hence, the alignment parameter A_{20} can be derived directly from the relative intensities. The expression for the alignment parameter in the LS coupling scheme is [16]

$$A_{20} = 2\frac{\sigma(^2P,0) - \sigma(^2P,1)}{\sigma(^2P,0) + 2\sigma(^2P,1)}\ . \tag{12.13}$$

In principle the magnetic substate excitation cross sections σ should be calculated separately for the two members of the doublet, i.e., for $1s(2s2p\ ^3\mathrm{P})\ ^2\mathrm{P}_a$ and $1s(2s2p\ ^1\mathrm{P})\ ^2\mathrm{P}_b$. However, within the LS coupling scheme, the calculated alignment is equal for the two members of the doublet. Ziem *et al.* performed plane wave Born (PWBA) calculations to determine the theoretical alignment parameter. Experiment and theory are compared in Fig. 12.15.

Although PWBA reproduced the tendency of the experimental data at high impact velocities, it failed to give account the absolute values. Moreover, the observed difference between the alignment parameters for the members of the doublet could not be explained within the given theoretical framework. Since double excitation was found to be non-negligible, probably higher-order processes are responsible for the discrepancies. A later experimental study performed at much higher impact velocities (95 MeV/u Ar^{18+} on Li) [124] provided much lower double excitation rates and a common alignment parameter for the two doublet lines in agreement with PWBA calculations.

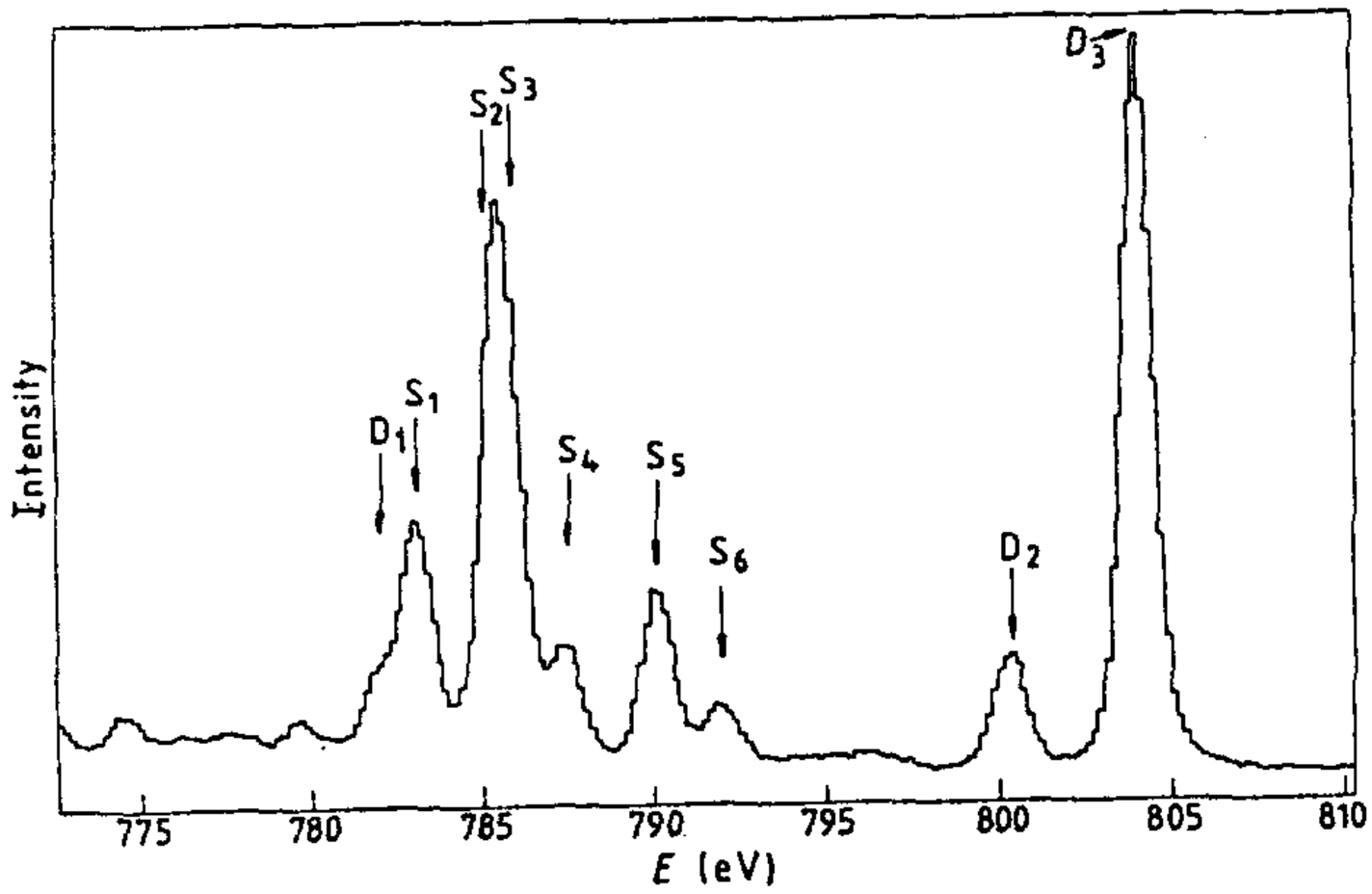

FIGURE 12.16 Ne K-LL Auger lines in the 782-805 eV energy region (5.5 MeV/u Ne^{3+} - Ne collision, 165° obsevation angle). The line denoted by S_4 belongs to the $1s2s^22p^5\ ^1P$ -$1s^22s^22p^3\ ^2P$ transition, while S_5 belongs to that of $1s2s^22p^5\ ^1P$ -$1s^22s^22p^3\ ^2D$. Reprinted from S. Ricz, I. Kádár, V.A. Shchegolev, D. Varga, J. Végh, D. Berényi, G. Hock, and B. Sulik, "Identification and angular distribution of the KL – $LL_{2,3}L_{2,3}$ satellites in the Ne K Auger spectra From the 5.5 MeV u^{-1} Ne^{3+} – Ne *collision process*" [61], with kind permission of IOP Publishing.

The first evidence of nonstatistical population and anisotropic satellite distribution in multiple ionized Li-like neon were provided by Matthews *et al.* [60] and Stolterfoht [23]. The 7-fold ionization of Ne is a complex collision. Without isotropic reference lines in the spectra, anisotropy parameters have not been determined.

Concerning nonstatistical vacancy production, the simplest case is to create one vacancy on a closed L-shell. The lowest Z element with closed L-shell is neon. For Ne, however, one gets an Auger transition at a single L-shell vacancy only if the K-shell is ionized. Hence, an anisotropic angular distribution of Auger lines is expected in the case of double ionization with one vacancy on the K-shell and another on the L_3 subshell. In a systematic study, Ricz *et al.* [61,62] measured the angular distribution of the K-LL satellite lines of neon doubly ionized by 5.5 MeV/u H^+, N^{2+}, Ne^{3+}, Ne^{10+} and Ar^{6+} ion impact investigating the projectile charge dependence of the alignment at a constant impact velocity. The projectile velocity dependence of the same process was studied by Takács *et al.* [125] in 0.7-2.1 MeV/u H^+ + Ne collisions. In both cases, the measurements were performed by means of the triple-pass multichannel spectrometer shown in Fig. 12.8. A typical spectrum containing the oxigen-like satellite region is shown in Fig. 12.16. As an example, the angular distribution of the lines denoted by S4 and S5 are plotted in Fig. 12.17. The solid curves are the fitted distributions.

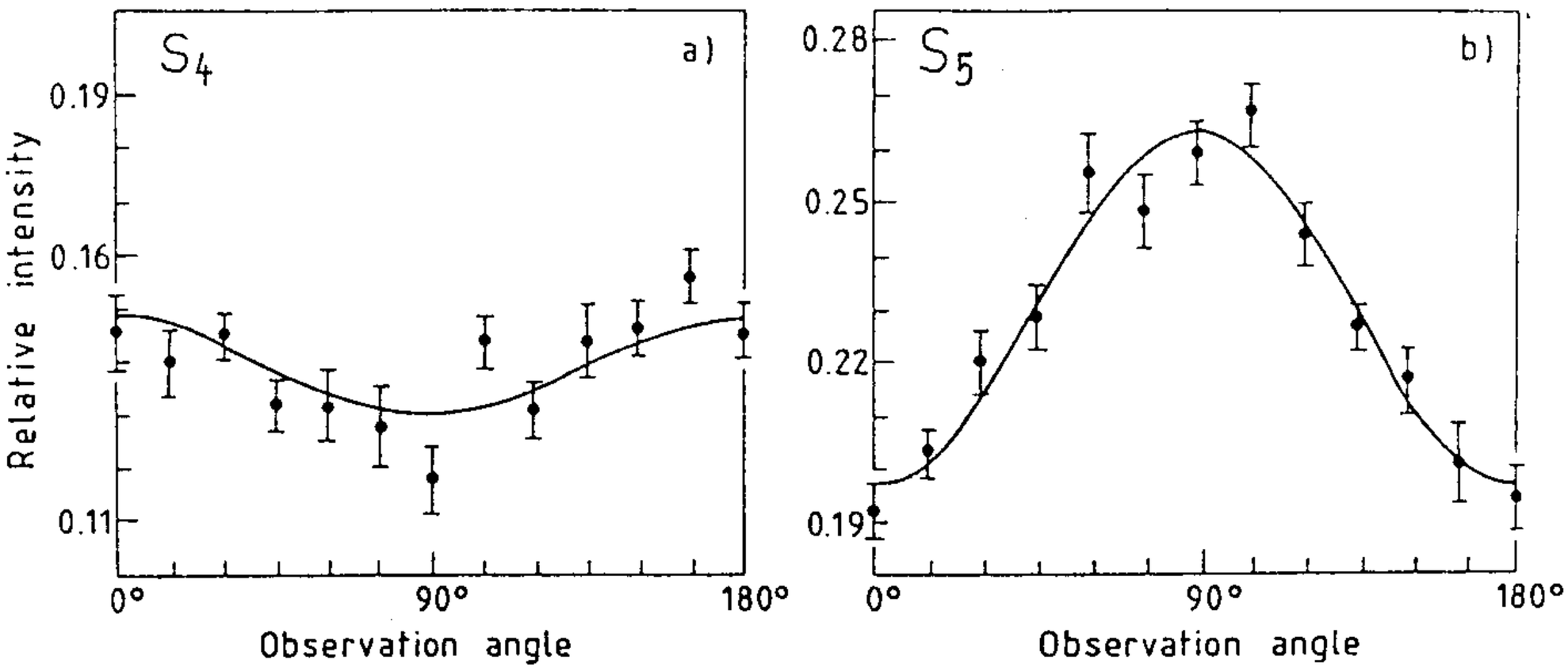

FIGURE 12.17 Angular distribution of the $1s2s^22p^5\ ^1$P -$1s^22s^22p^3\ ^2$P (S_4) and the $1s2s^22p^5\ ^1$P -$1s^22s^22p^3\ ^2$D (S_5) Ne Auger transitions. (5.5 MeV/u Ne^{3+} - Ne collision) The solid curve is the fitted angular distribution. Reprinted from S. Ricz, I. Kádár, V.A. Shchegolev, D. Varga, J. Végh, D. Berényi, G. Hock, and B. Sulik, "Identification and angular distribution of the KL – $LL_{2,3}L_{2,3}$ satellites in the Ne K Auger spectra From the 5.5 MeV u^{-1} Ne^{3+} – Ne collision process" [61], with kind permission of IOP Publishing.

An interesting point here is that different Auger lines have different α_k values. They can have even opposite sign. If two lines originate from the same initial state, i.e., the alignment parameter is strictly common for the two transitions, then the ratio of the two α_k values is a *measured* quantity. Calculated α_k values are very sensitive on the theoretical methods if more than one partial wave contributes to the transition [10,16]. Therefore, the measured angular distributions provide important information for atomic structure and Auger theories independently of the particular collision process. A detailed analysis of coherence and correlation in the Ne K-LL Auger decay, based on the above experimental data [61,62,125], has recently been performed by Kabachnik *et al.* [10].

Like for the excitation of Li, first order theories within the LS coupling scheme provide one common alignment parameter A_{20} for the L_3 subshell in the ionization case, too. Hence, one may expect that by means of realistic α_k values *all* the measured Auger lines provide the same alignment parameter. For most of the investigated lines, Ricz *et al.* [61,62] confirmed this within the experimental error. It supports the conclusion that the LS coupling scheme is applicable for K+L vacancy states of neon.

Another important feature of the K+L-shell double ionization is that the characteristic impact-parameter region is of the order of the K-shell radius and small compared to that of the L-shell. Therefore, L-shell ionization is governed by small impact parameter collisions. Hence, in Eq. (12.13) one

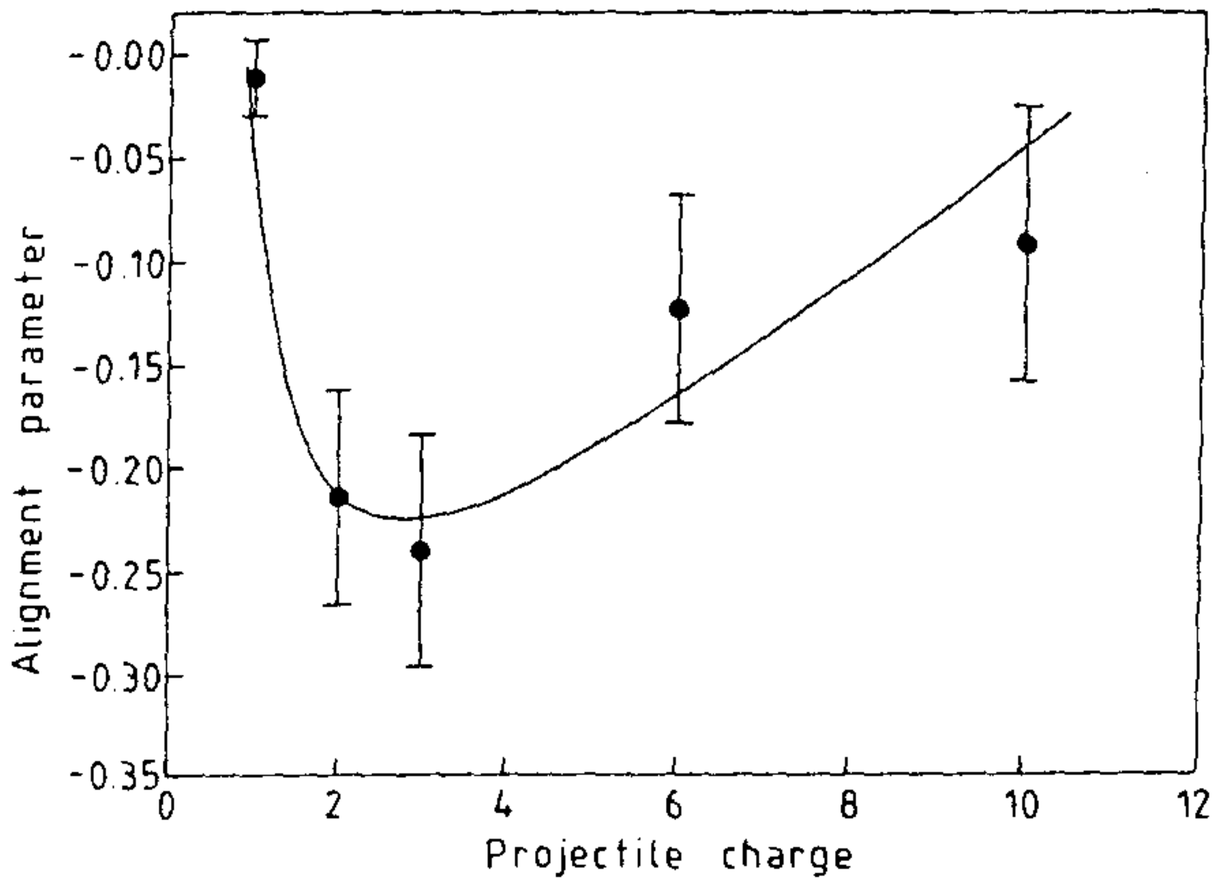

FIGURE 12.18 Alignment parameter versus projectile ion charge for the $1s2s^22p^5\ ^{1,3}$P state of Ne in 5.5 MeV/u H^+, N^{2+}, Ne^{3+}, Ar^{6+} and Ne^{10+} - Ne collisions. The solid line is drawn to guide the eye. Reprinted from S. Ricz, J. Végh, I. Kádár, B. Sulik, D. Varga and D. Berényi, "Fast multicharged ion-induced satellite Auger electron angular distributions" [62], with kind permission of Elsevier Science - NL, Sara Burgerhartstraat 25, 1055 KV Amsterdam, The Netherlands..

may replace cross sections by ionization probabilities. The method can be considered as a differential measurement providing more information about fine details of the collision mechanism than total cross section studies do.

The results of the systematic study of Ricz *et al.* [61,62] are summarized in Fig. 12.18. A strong dependence of the alignment on the projectile charge has been found. First order semiclassical calculations predict a common value of the alignment parameter, namely -0.3 for all projectiles (see also Fig. 12.19) [125]. This is in fairly good agreement with the N^{2+} and Ne^{3+} data. For H^+ projectile, the contribution of the entirely isotropic shake-off mechanism is not negligible. When taking it into account, A_{20} is reduced to -0.07 for H^+ [125]. It is still significantly larger than the experimental value. At higher charge states, higher-order effects could be responsible for the decreasing absolute value of the alignment parameter.

The experimental point for H^+ in Fig. 12.18 is the same as that displayed by a full symbol in Fig. 12.19, where the projectile velocity dependence is displayed in proton-neon collision [125]. In Fig. 12.19 it is clearly seen that using realistic atomic wave functions and taking into account the contribution of the isotropic shake-off ionization mechanism, a good agreement has been achieved between theory and experiment. The only exception is the 5.5 MeV point where theory provides much stronger alignment than the experiment.

For heavier targets, a vacancy in the closed L shell can decay by L-MM, L-MN, etc. Auger transitions. Hence the alignment of *single ionized* atoms

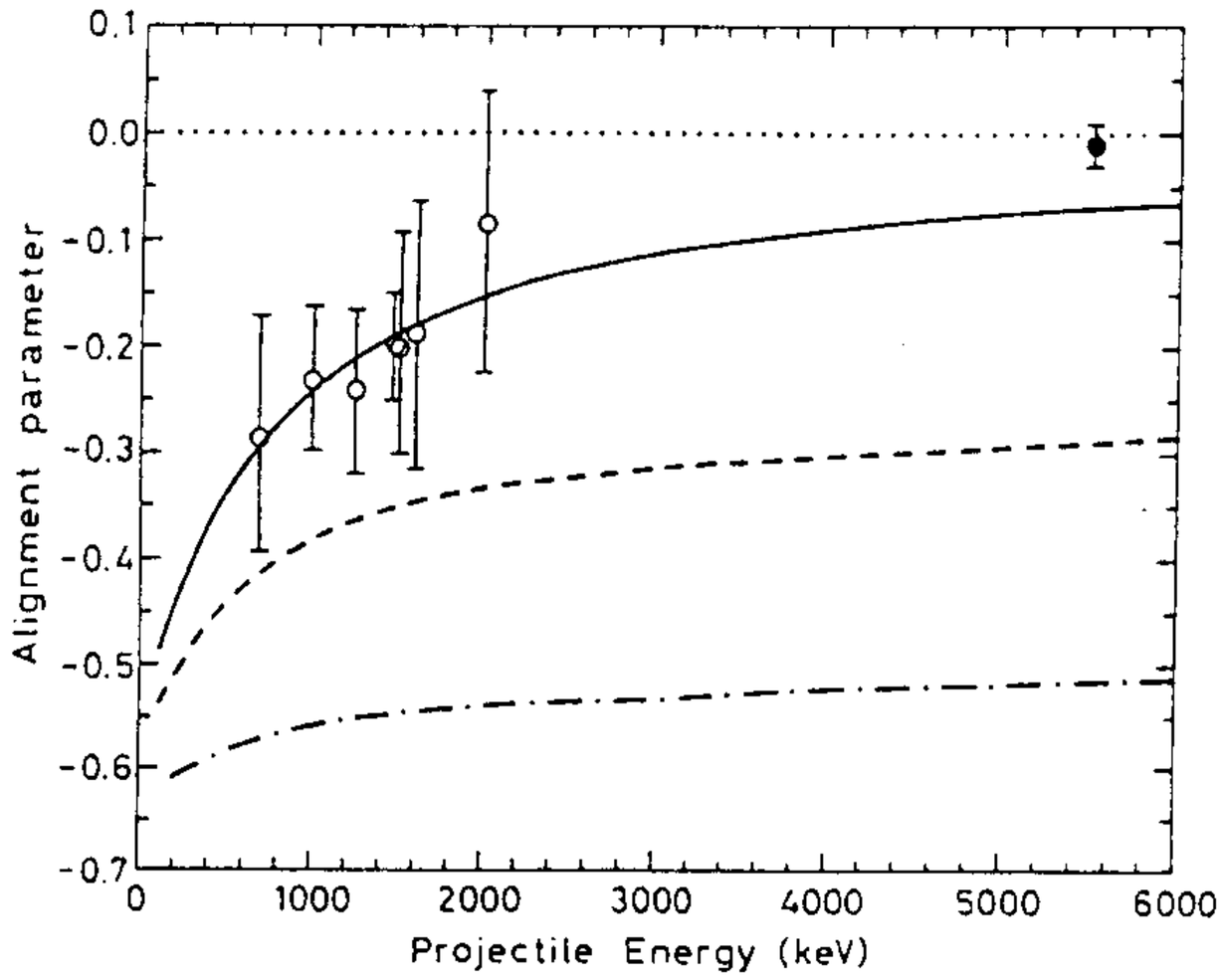

FIGURE 12.19 The projectile energy dependence of the alignment parameter for the $1s2s^22p^5\ ^{1,3}$P state of Ne in H^+- Ne collisions. Dot-dashed line, the results of the calculations within the framework of the straight-line semiclassical approximation with hydrogen-like wave functions; dashed line, the same calculation with Hartree-Slater wave functions; solid line, Hartree-Slater results combined with the shake-off contribution. From ref. [125].

can also be studied by Auger spectroscopy. It is noted here that for heavier elements, this single L-vacancy alignment is usually studied by X-ray spectroscopy. Since here the total cross sections enter into Eq. (12.13), the alignment parameter provides information about average quantities. In the high impact velocity region, convenient for high resolution Auger studies, the anisotropy is usually small. If, however, different vacancy production mechanisms are distinguished, the partial alignment parameters can be very large. This is demonstrated in Fig. 12.20 [63,64].

The alignment of the L_3 subshell induced by electron capture for proton impact has been studied by Sarkadi *et al* [63] for Ar target, and by Gutenkunst *et al* [64] for Mg target in wide impact energy regions. Both experiments were based on the measurement of the angular distribution of the L-MM Auger electrons (diagram lines, see Fig. 12.6) in coincidence with the outgoing neutral H atoms.

In both cases, strong and velocity dependent alignment has been found for the capture process. The total alignment measured without coincidence is nearly zero in the investigated impact energy region, in good agreement with PWBA-based effective alignment calculations [63]. It is clearly seen that neither of the displayed capture theories agree with the experimental data quantitatively. Only the Oppenheimer-Brinkmann-Kramers (OBK) approximation reproduces the tendencies for both collision systems and provides a qualitative agreement with the Mg data. Fig. 12.20 clearly demonstrates how

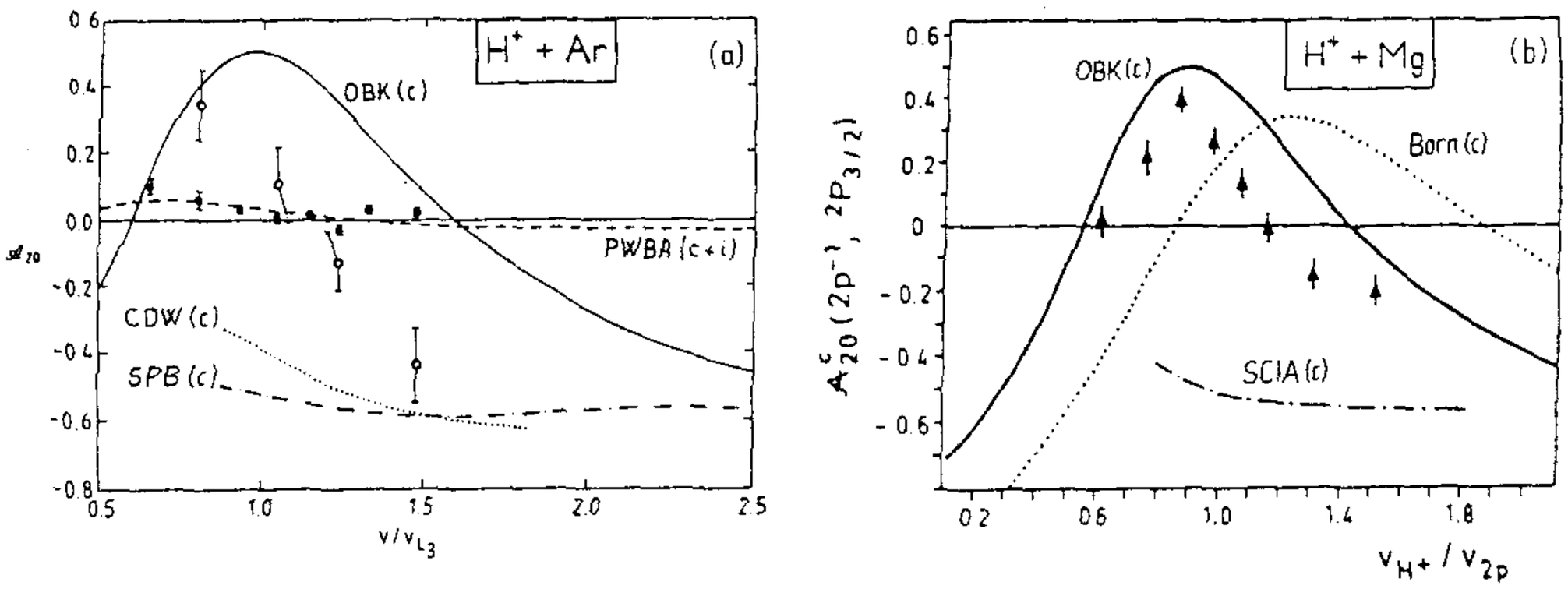

FIGURE 12.20 L3-subshell alignment parameters for proton bombardement as a function of the relative collision velocity: **a)** for Ar target [63], open circles: results obtained by the coincidence detection of the Auger electrons with the outgoing H° atoms; full circles: results of non-coincidence measurements; lines: theoretical calculations. **b)** for Mg target [64], symbols: corrected coincidence data for the electron capture process; lines: theoretical calculations. Part **a** is reprinted from L. Sarkadi, T. Vajnai, J. Pálinkás, Á Kövér, J. Végh and T. Mukoyama, "L_3-subshell alignment of Ar following charge-changing collisions with protons" [63], with kind permission from IOP Publishing Limited. Part **b** is reprinted from A. Gutenkunst, S. Zuccati and W. Mehlhorn, "L_3 – subshell alignment of magnesium after electron capture by protons" [64], with kind permission from IOP Publishing Limited.

important it is to perform differential experiments to really test theories.

12.4.3 Post-collision interaction

In a general sense, post collision interaction (PCI) is a time-dependent Coulomb interaction between the collision fragments produced in an atomic collision. Concerning the Auger process, the manifestations of PCI are line shift, line-shape distortion and line-intensity variation. Since the first observation of the phenomenon by Barker and Berry [44] in slow ion-atom collisions, it has been studied extensively both experimentally and theoretically (see e.g., the reviews [67,126] and references therein). PCI can be significant for the majority of atomic collision systems, like photon, electron, or ion impact. Detailed information about the post-collision interaction can be extracted from high-resolution Auger spectra by analyzing the shape of the individual lines.

Post collision interaction has two important aspects. The basic research aspect is that the study of the PCI effect provides valuable data relevant to three and many-body collision theories. The practical aspect is connected to the precise determination of the position and the intensity of the Auger lines.

Accurately known PCI line-shapes can improve the evaluation procedure and help to extract reliable spectroscopic information from the measured spectra.

For an outgoing heavy charged projectile, the PCI-distorted Auger line-shape can be well treated within the framework of a semiclassical theory [127–129]. A fully quantum mechanical continuum distorted wave (CDW) treatment of the PCI effect in ion-atom collisions has been developed by Barrachina and Macek [130]. For fast collisions, the two theories predict very similar dependence of the Auger line-shape on the impact energy and the Auger electron emission angle in good agreement with experiment. It is noted here that the CDW theory predicts not only line shape but also intensity variation due to the focusing Coulomb attraction exerted by the projectile on the Auger electron ejected into the forward direction. Conclusive experimental evidence and theoretical explanation of the Coulomb focusing effect in slow He+ - He collisions was presented by Swenson *et al* [131]. Experimental indications of intensity variations in the region where the velocity of the Auger electron $\mathbf{v}_a$ and that of the outgoing projectile $\mathbf{v}_p$ are nearly equal were recently reported for Ne target [67].

If the projectile-target separation is large at the moment of the Auger decay and the projectile-electron relative velocity $\mathbf{v}_p - \mathbf{v}_a$ is not too small, the semiclassical theory leads to an approximate analytical expression for the line-shape

$$P(E) = \frac{\Gamma^a_{if}/2\pi}{(E-E_a)^2 + (\Gamma^n/2)^2} \frac{\pi\xi}{\sinh(\pi\xi)} \exp\left(2\xi \arctan\frac{2(E_a-E)}{\Gamma^n}\right). \quad (12.14)$$

Here the Lorenzian line-shape of Eq. (12.6) is distorted by a factor containing the asymmetry parameter ξ. The connection between the asymmetry parameter and the line shift is linear

$$\Delta E = \Gamma^n \xi/2. \quad (12.15)$$

The asymmetry parameter is expressed by the Auger electron velocity and the projectile velocity

$$\xi = \frac{Z_p}{v_p}\left(\frac{v_p}{|\mathbf{v}_p - \mathbf{v}_a|} - 1\right). \quad (12.16)$$

It is clearly seen that the predicted asymmetry depends on the emission angle of the Auger electron. Moreover, there is a singularity at $\mathbf{v}_p = \mathbf{v}_a$, i.e., where the outgoing projectile and the Auger electron leave the collision region in the same direction, with the same velocity. At the singularity, the energy of the Auger electron is equal to the so called cusp electron energy ($E_{cusp} = v_p^2/2$). The above simple formulas are not valid near the singularity, but they correctly show many characteristic features of the PCI effect.

Under ion impact, PCI is a rather complicated effect with strong impact velocity and angular dependence. The number of outgoing charged particles

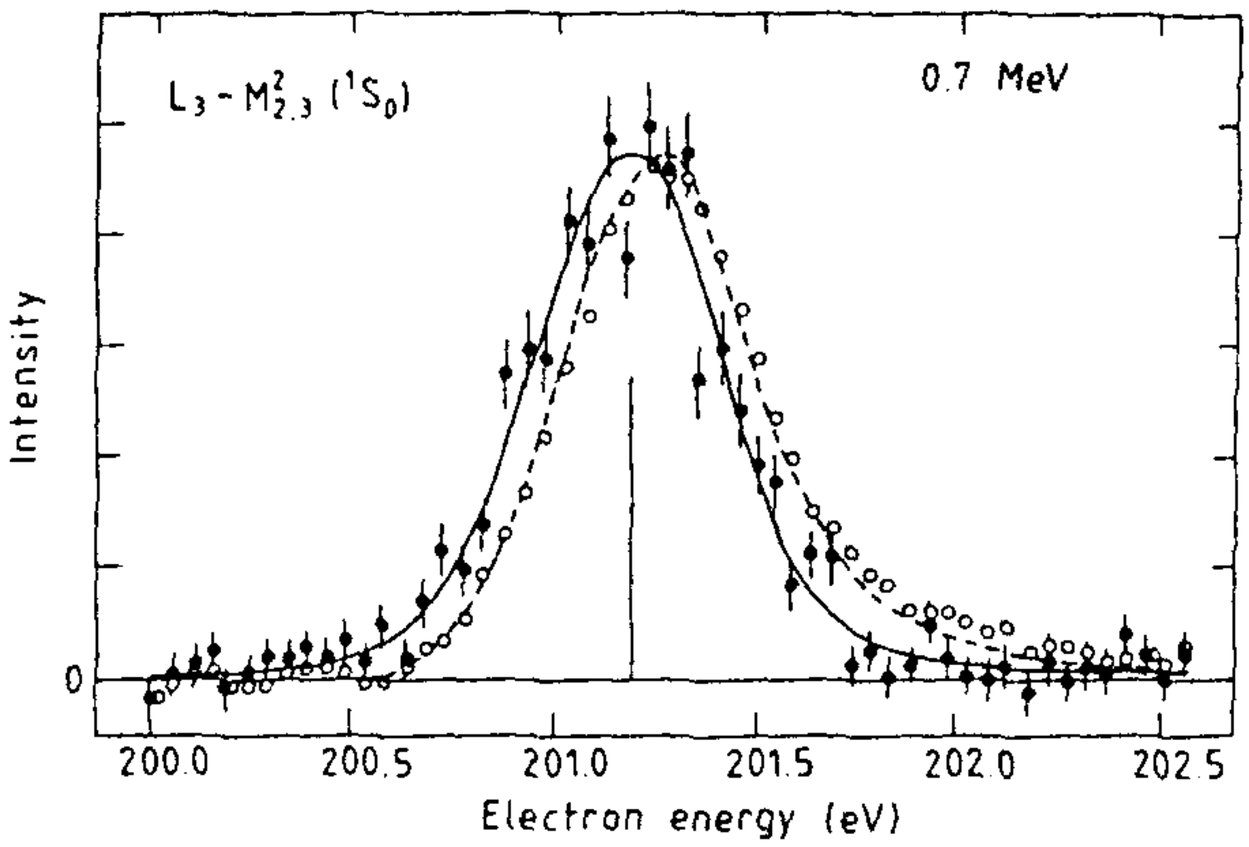

FIGURE 12.21 Electron spectra of the L_3-$M_{2,3}M_{2,3}$ $^1S_0$ Auger line of argon excited by 0.7 MeV protons and observed at 0°. The two spectra have been obtained in the same experiment by detecting the Auger electrons in coincidence with the outgoing H^0 atoms (full symbols) and without the coincidence condition (open symbols). The amplitudes of the peaks are normalized to each other after background substraction. The curves through the experimental points are results of computer fitting based on the lineshape given by Eq. (12.14). Reprinted from L. Sarkadi, T. Vajnai, J. Végh and Á Kövér, "A new method for measurement of post-collision interaction effects for p on Ne collisions" [68], with kind permission of IOP Publishing Limited.

can be large. It was shown by Ricz *et al.* [132] that at high impact velocities where the PCI effect between the outgoing projectile and the Auger electron is negligible, directly ionized electrons still provide a significant PCI distortion of the Auger lines. However, there is a unique situation, namely the electron capture from an inner shell of the target by a singly charged projectile. In this case the Auger electron is the only outgoing charged particle. Accordingly, *no* post-collision effect is expected. The undistorted Auger line shape and transition energy can be directly measured and compared to those distorted by the PCI effect. The coincidence study of Sarkadi *et al.* [68] clearly demonstrates the effect of PCI for 0.7 MeV proton-argon collision around 0° as shown in Fig. 12.21. The Auger line measured in coincidence with the outgoing neutral projectiles provides a symmetric shape. In contrast, the line measured without coincidence condition, i.e., which belongs predominantly to ionization, is shifted to higher energies and has an asymmetric shape.

It is noted here that there exists an alternative model-independent method to determine the natural line shape and PCI distortions. It is based on the fact that the line shape of a long-living metastable Auger transition is practically not affected by PCI. The outgoing charge fragments are typically far away when the Auger emission occurs. Since the natural width of the metastable states is much smaller than that of the other initial states, these

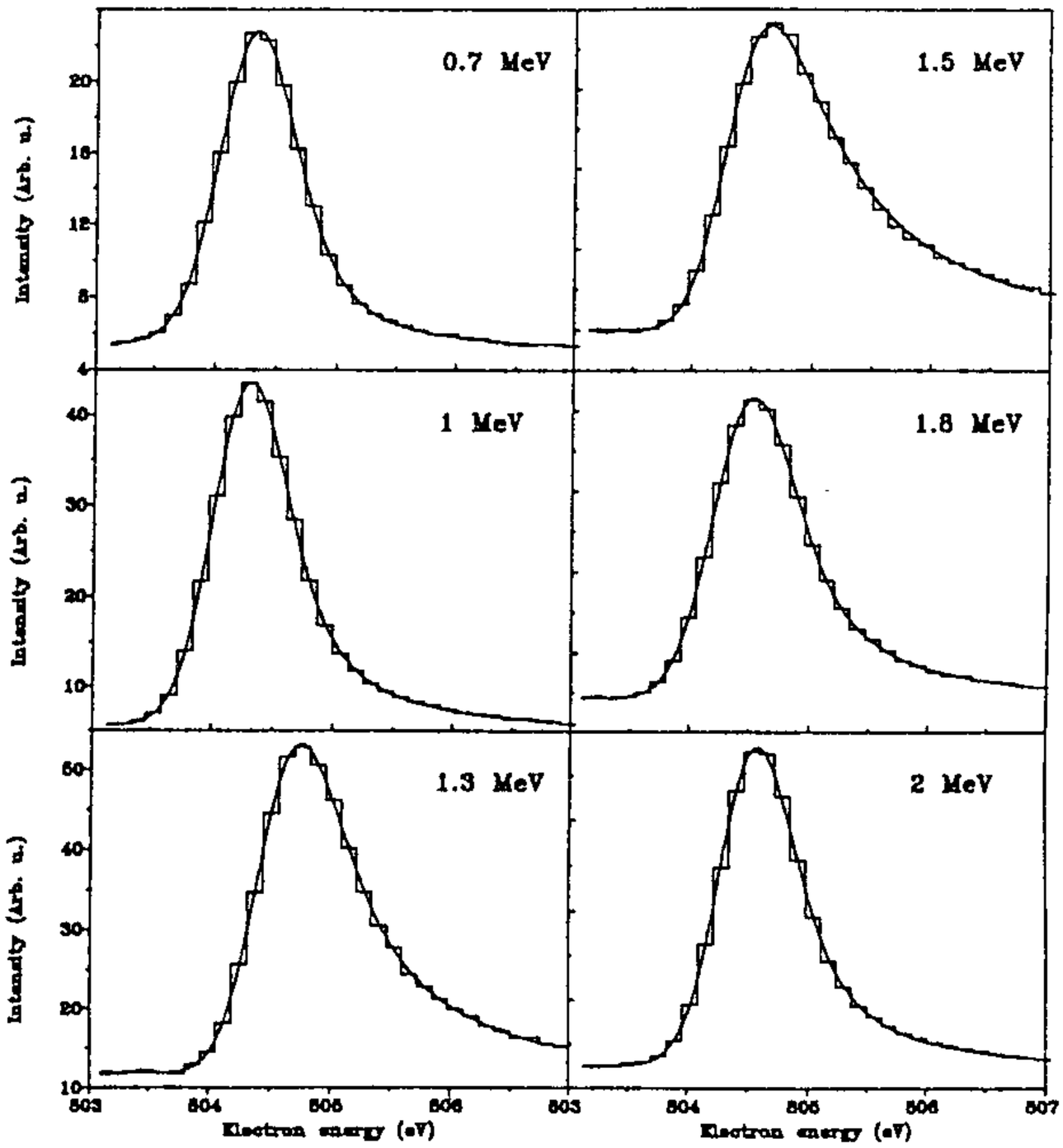

FIGURE 12.22 The Ne K-$L_{2,3}L_{2,3}$ $^1D_2$ Auger line excited by proton bombardment at different impact energies at 0° observation angle. The curves through the experimental points are results of computer fitting with use of the distribution given by Eq. (12.14). Reprinted from E. Takács, L. Sarkadi, S. Ricz, B. Sulik and L. Tóth, "Measurement of post-collision interaction effects for p on Ne collisions" [66], with kind permission of IOP Publishing Limited.

lines can be used for the experimental determination of the spectrometer function [106,132]. Hence, the shape and asymmetry of the other lines in the spectrum can be reliably determined during the fitting procedure.

An experimental study of the PCI effect around the singularity predicted by Eq. (12.16) was performed by Takács *et al.* [66]. The distortion of the Ne K-$L_{2,3}L_{2,3}$ $^1D_2$ diagram Auger line (E_a = 804.5 eV) has been studied by proton bombardment in the energy range of 0.7-2.0 MeV at different polar emission angles by means of the triple pass spectrometer. Since the cross section of the electron capture to continuum (ECC) process was fairly small for the considered collision system, background substraction could easily be done even in the zero degree spectra. The proton energy belonging to the cusp energy of 804.5 eV is 1477 keV. The spectra collected at 0° observation angle are shown in Fig. 12.22 after background substraction. The resonance-like behavior of line-shift and asymmetry around the expected singularity at 1477 keV is clearly demonstrated. It is also seen that the semiclassical theory

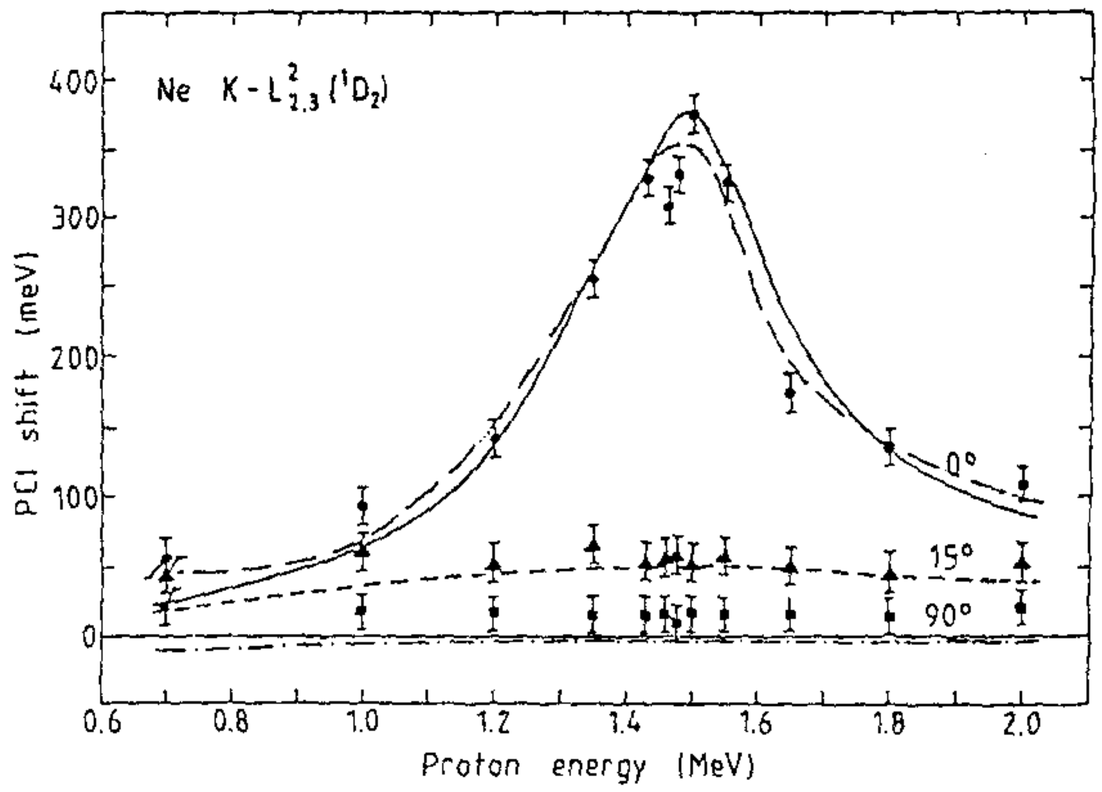

FIGURE 12.23 The dependence of the PCI shift of the K-$L_{2,3}L_{2,3}$ $^1D_2$ Auger line of neon on the impact proton energy at 0°, 15°, and 90° observation angles. The experimental data in the figure have been obtained by fitting the lines with Eq. (12.14) and deriving the line-shift from the asymmetry parameter by the help of Eq. 12.15. The full curve represents the theory of van der Straten and Morgenstern [128]. The broken curve represents the results obtained using the theory of Barrachina and Macek [130]. An integration over the finite solid angle of the spectrometer is included in the theoretical curves. Reproduced from E. Takács, L. Sarkadi, S. Ricz, B. Sulik and L. Tóth, "Measurement of post-collision interaction effects for p on Ne collisions" [66], with kind permission of IOP Publishing Limited.

(Eq.(12.14)) provides an excellent fit (solid line) of the experimental data (step curves).

The results are summarized in Fig. 12.23, showing the dependence of the PCI shift of the K-$L_{2,3}L_{2,3}$ $^1D_2$ Auger line of neon on the proton impact energy at 0°, 15°, and 90° observation angles. It is clearly seen that the resonant like behavior is quantitatively reproduced by both semiclassical and CDW theories at 0° and 15° observation angles. Of course, an integration over the finite solid angle of the spectrometer is included in the theoretical curves. The disagreement at 90° can be identified as PCI effect originating from the directly ionized electrons (see ref. [132]).

The level of our understanding related to the PCI effect in fast ion-atom collisions seems to be rather satisfactory concerning the adequate line-shapes for spectroscopic applications. Questions remain open, however, e.g., in connection with the observed intensity variations at high impact velocities [67] which cannot be reproduced by the present theories.

ACKNOWLEDGMENTS

The authors would like to thank T. Zouros, D. Varga, L. Sarkadi, Á. Kövér, J. Végh and S. Ricz for their critical reading of the manuscript and their valu-

able comments. This work was supported by the Hungarian National Science Foundation (OTKA, Contract No. T 016636) and the Hungarian-German Intergovernmental ST Cooperation Programme (Contract No. B.129)

REFERENCES

1. P. Auger, Compt. Rend. **177**, 169 (1923); **180**, 65 (1925).
2. P. Auger, J. Phys. Radium **6**, 205 (1925).
3. G. Wentzel, Z. Phys. **43**, 524 (1927).
4. P.G. Burke, in *Advances in Atomic and Molecular Physics*, Vol. 4, eds. D.R. Bates and I. Estermann (Academic Press, New York, 1968) p. 173.
5. E.H.S. Burhop and W.N. Asaad, in *Advances in Atomic and Molecular Physics*, Vol. 8 (Academic Press, New York, 1972) p. 164.
6. D. Chattarji, *The Theory of Auger Transitions* (Academic Press, New York, 1976).
7. E.J. McGuire, in *Atomic Inner-Shell Processes*, Vol. I, ed. B. Crasemann (Academic Press, New York, 1975) p. 293.
8. T. Åberg and G. Howat, in *Handbuch der Physik*, Vol. 31, eds. S. Flgge and W. Mehlhorn (Springer Verlag, Berlin, 1982) p. 469.
9. N. Stolterfoht, Physics Reports, **146**, 317 (1987).
10. N. M. Kabachnik, J. Tulkki, H. Aksela and S. Ricz, Phys. Rev. A **49**, 4653 (1994).
11. G.N. Ogurtsov, Rev. Mod. Phys. **44**, 1 (1972).
12. A. Niehaus, in *Atomic Inner-Shell Physics*, ed. B. Crasemann (Plenum Press, New York, 1985) p. 377.
13. M.E. Rudd and J. Macek, in *Case Studies in Atomic Physics*, Vol. 3, eds. E.W. McDaniel and M.R.C. McDowell (North-Holland, Amsterdam, 1973) p. 47.
14. K.D. Sevier, *Low Energy Electron Spectrometry* (J. Wiley Interscience, New York, 1972).
15. W. Mehlhorn, *Electron Spectrometry of Auger and Autoionizing States: Experiment and Theory*, Lecture Notes, University of Aarhus (1978) unpublished.
16. W. Mehlhorn, in *Atomic Inner-Shell Physics*, ed. B. Crasemann (Plenum Press, New York, 1985) p. 119.
17. W. Mehlhorn, in *X-ray and Inner Shell Processes* (AIP Conf. Proc. 215), eds. T.A. Carlson, M.O. Krause and S.T. Manson (AIP, New York, 1990) p. 465.
18. D.L. Matthews, in *Methods of Experimental Physics*, Vol. 17, ed. P. Richard (Academic Press, New York, 1980) p. 433.
19. D. Berényi, in *Advances in Electronics and Electron Physics*, Vol. 56 (Academic Press, New York, 1981) p. 411.
20. D. Berényi, in *X-Ray Spectroscopy in Atomic and Solid State Physics* NATO-ASI Series Vol. B-187, eds. J. Gomes Ferreira and M.T. Ramos (Plenum Press, New York, 1988) p. 25.
21. N. Stolterfoht, J. El. Spectrosc. Relat. Phenom. **67**, 309 (1993).

22. N. Stolterfoht, Physica Scripta **T51**, 36 (1994).
23. N. Stolterfoht, in *Scientific and Industrial Applications of Small Accelerators*, IEEE Trans. Nucl. Sci. 76CH1175-8 NTS (1976) p. 311.
24. N. Stolterfoht, *Topics in Current Physics*, Vol. 5: *Structure and Collisions of Ions and Atoms*, ed. I.A. Sellin (Springer Verlag, Berlin, 1978) p. 155.
25. N. Stolterfoht, in *Fundamental Processes in Energetic Atomic Collisions*, eds. H.0. Lutz, J.S. Briggs and H. Kleinpoppen (Plenum Press, New York, 1983) p. 295.
26. R. Mann, F. Beyer and F. Folkmann, in *XII Intern. Conf. on the Physics of Electronic and Atomic Coliisions, Invited Papers*, ed. S. Datz (North-Holland, Amsterdam, 1982) p. 683.
27. M.E. Rudd, Y.-K. Kim, D.H. Madison and T.J. Gay, Rev. Mod. Phys. **64**, 441 (1992).
28. J.D. Garcia, R.J. Fortner and T.M. Kavanagh, Rev. Mod. Phys. **45** 111 (1973).
29. Q.C. Kessel and B. Fastrup, in *Case Studies in Atomic Physics*, Vol. 3, eds. E.W. McDaniel and M.C. McDowell (North-Holland, Amsterdam, 1973) p. 137.
30. W.E. Meyerhof and K. Taulbjerg, Ann. Rev. Nucl. Sci. **27**, 279 (1977).
31. J.S. Briggs and J.H. Macek, in *Advances in Atomic, Molecular and Optical Physics*, Vol. 28, eds. D. Bates and B. Bederson (Academic Press, New York, 1990) p. 1.
32. J.H. McGuire, in *Advances in Atomic, Molecular and Optical Physics*, Vol. 29, eds. D. Bates and B. Bederson (Academic Press, New York, 1992) p. 217.
33. K. Siegbahn, C. Nordling, G. Johannson, J. Hedman, P.F. Heden. K. Hamrin, U. Gelius. T. Bergmark, L.O. Werme, R. Manne and Y. Baer, *ESCA Applied to Free Molecules* (North-Holland, Amsterdam, 1968).
34. M.O. Krause, in *Atomic Inner Shell Processes*, Vol. II, ed. B. Crasemann (Academic Press, New York, 1975) p. 33.
35. T.A. Carlson, *Photoelectron and Auger Spectroscopy* (Plenum Publishing Corporation, New York, 1975).
36. K. Siegbahn et al., *ESCA-Atomic, Molecular, and Solid-State Structure by Means of Electron Spectroscopy*, Nova Acta Reg. Soc. Sci. Uppsallienis, Ser. IV (1967) p. 20.
37. J.C. Riviere, *Surface Analytical Techniques* (Clarendon Press, Oxford, 1990).
38. A. Niehaus, Physics Reports **186**, 149 (1990).
39. W. Mehlhorn, Phys. Lett. **21**, 155 (1966).
40. W. Mehlhorn, Z. Physik **160**, 247 (1960).
41. H.W. Berry, Phys. Rev. **121** 1714 (1961).
42. T.A. Carlson and M.O. Krause, Phys. Rev. Lett. **14**, 390 (1965).
43. M.E. Rudd, Phys. Rev. Lett. **13**, 503 (1964); **15**, 580 (1965).
44. B.R. Barker and H.W. Berry, Phys. Rev. **151**, 14 (1966).
45. M.E. Rudd, T. Jorgensen Jr. and D.J. Volz, Phys. Rev. Lett. **16**, 929 (1966); and Phys. Rev. **151**, 28 (1966).
46. Yu.S. Gordeev and G.N. Ogurtsov, Zh. Eksp. Teor. Fiz. **60**, 2051 (1971) [Sov. Phys.-JETP **33** 1105 (1971)].

47. R.K. Cacack, Q.C. Kessel and M.E. Rudd, Phys. Rev. A **2**, 1327 (1970).
48. D.L. Matthews, B.M. Johnson, J.J. Mackey and C.F. Moore, Phys. Rev. Lett. **31**, 1331 (1973).
49. D. Burch, P. Richard and R.L. Blake, Phys. Rev. Lett. **26**, 26 (1971).
50. N. Stolterfoht, D. Schneider, R. Mann and F. Folkmann, J. Phys. B **10**, L281 (1977).
51. D. Schneider, M. Prost, R. DuBois and N. Stolterfoht, Phys. Rev. A **25**, 3102 (1982).
52. R. Mann and F. Folkmann, J. Physique **40**, CI-236 (1979).
53. C. Woods, R.L. Kauffman, K. Jamison, N. Stolterfoht and P. Richard, Phys. Rev. A **12**, 1393 (1975).
54. I. Kádár, S. Ricz, V.A. Shchegolev, B. Sulik, D. Varga, J. Végh, D. Berényi and G. Hock, J. Phys. B **18**, 275 (1985).
55. T. Matsuo, J. Urakawa, A. Yagishita, Y. Awaya, T. Kambara, M. Kase and H. Kumagai, J. Phys. B **16** L239 (1983).
56. I. Kádár, S. Ricz, V.A. Shchegolev, D. Varga, J. Végh, D. Berényi, G. Hock, and B. Sulik, Phys. Lett. A **115**, 439 (1986).
57. I. Kádár, S. Ricz, J. Végh, B. Sulik, D. Varga and D. Berényi, Phys. Rev. A **41**, 3518 (1990).
58. B. Sulik, I. Kádár, S. Ricz, D. Varga, J. Végh, G. Hock and D. Berényi, Nucl. Instr. Meth. B **28**, 509 (1987).
59. P. Ziem, W.H.E. Schwarz, D. Ridder and R. Schilling, Japanese Journal of Applied Physics, **17**, Supplement 17-2, 367 (1978).
60. D.L. Matthews, R.J. Fortner, D. Schneider and C.F. Moore, Phys. Rev. A **14** 1561 (1976).
61. S. Ricz, I. Kádár, V.A. Shchegolev, D. Varga, J. Végh, D. Berényi, G. Hock, and B. Sulik, J. Phys. B **19**, L411 (1986).
62. S. Ricz, J. Végh, I. Kádár, B. Sulik, D. Varga and D. Berényi, Nucl. Instr. Meth. B **61**, 411 (1991).
63. L. Sarkadi, T. Vajnai, J. Pálinkás, Á Kövér, J. Végh and T. Mukoyama, J. Phys. B **23**, 3643 (1990).
64. A. Gutenkunst, S. Zuccati and W. Mehlhorn, J. Phys. B **27**, 533 (1994).
65. P.W. Arcuni, Phys. Rev. A **33**, 105 (1986).
66. E. Takács, L. Sarkadi, S. Ricz, B. Sulik and L. Tóth, J. Phys. B **24**, L381 (1991).
67. S. Ricz, Nucl. Intr. Meth. B **86**, 119 (1994).
68. L. Sarkadi, T. Vajnai, J. Végh and Á Kövér, J. Phys. B **24**, L381 (1991).
69. H. Ishii, Y. Iketaki, T. Watanabe, T. Takayanagi, K. Wakiya and H. Suzuki, Phys. Rev. A **43**, 134 (1991).
70. Birgit Lohmann, J. Phys. B **24**, L249 (1991).
71. Q. Zengh, A.K. Edwards, R.M. Wood and M.A. Mangan, Phys. Rev. A **52**, 3940 (1995).
72. C.D. Caldwell and M.O. Krause, Phys. Rev. A **47**, R759 (1993).
73. D.H. Lee, B.M. Johnson, N.A. Guardala, J.L. Price, G.A. Glass, M.F. Stumborg and K.W. Jones, Nucl. Instr. Meth. B **79**, 261 (1993).

74. H.A. Bethe and R. Jackiw, *Intermediate Quantum Mechanics* (W.A. Benjamin Inc., New York, 1968) p. 135.
75. N. Stolterfoht, H. Gabler and U. Leithauser, Phys. Lett. A **45**, 351 (1973).
76. D. Coster and R.L. Kronig, Physica **2**, 13 (1935).
77. T.A. Carlson and M.O. Krause, Phys. Rev. Lett. **17**, 1079 (1965).
78. M.O. Krause, T.A. Carlson and W.E. Moddeman, J. de Phys. (Paris) **32** C4-139 (1971).
79. V.V. Afrosimov, Yu.S. Gordeev, A.N. Zinoviev, D.H. Rasulov and A.P. Shergin, *IX Intern. Conf. on the Physics of Electronic and Atomic Collisions, Abstracts*, eds. J.S. Risley and R. Geballe (University Press, Seattle, 1975) p. 1068.
80. T. Åberg and J. Utriainen, Phys. Rev. Lett. **22**, 1346 (1969).
81. P. Richard, J. Oltjen, K.A. Jamison, R.L. Kaufmann, C.W. Woods and J.M. Hall, Phys. Lett. **54** A, 169 (1975).
82. C.E. Kuyatt, in *Methods of Experimental Physics*, Vol. 7A, eds. B. Bederson and W.L. Fite (Academic Press, New York, 1968) p. 1.
83. I. Kádár, D. Berényi, S. Ricz, B. Sulik, D. Varga and J. Végh, in *Spectroscopy and Collisions of Few-Electron Ions*, eds. M. Ivascu, V. Florescu and V. Zoran (World Scientific, Singapoore, 1989) p. 434.
84. J.C. Nickel, P.W. Zetner, G. Shen and S. Trajmar, J. Phys. E: Sci. Instrum. **22**, 730 (1989).
85. J. Végh, I. Kádár, S. Ricz, B. Sulik, D. Varga and G. Székely, Nucl. Instr. Meth. A **281**, 605 (1989).
86. D. Roy and J.-D. Carette, Canadian J. Phys. **49**, 2138 (1971).
87. P. Dahl, *Introduction to Electron and Ion Optics*, (Academic Press, New York, 1975).
88. B. Wannberg, U. Gelius and K. Siegbahn, J. Phys. E **7**, 149 (1974).
89. V.P. Afanasev and S.J. Javor, Zh. Tech. Fiz. **45** 1137 (1975).
90. E.H.A. Granneman and M.J. Van der Wiel, in *Handbook of Synchrotron Radiation*, Vol. 1, ed. E.E. Koch (North Holland, Amsterdam, 1983) pp. 369-462.
91. R.C.G. Leckey, J. El. Spectr. Rel. Phenom. **43**, 183 (1987).
92. D. Roy and D. Tremblay, Rep. Prog. Phys. **53**, 1621 (1990).
93. G.A. Harrower, Rev. Sci. Instr. **26**, 850 (1955).
94. T.S. Green and G.A. Proca, Rev. Sci. Instr. **41**, 1409 (1970).
95. A.L. Hughes and V.J. Rojanski, Phys. Rev. **34**, 284 (1929).
96. F. Tofoletto, R.C.G. Leckey and J.D. Ridley, Nucl. Instr. Meth. B **12**, 282 (1985).
97. G. Richmond, G. Bagley and T. Reddish, in *XVIII. Int. Conf. on the Physics of Electronic and Atomic Collisions, Abstracts*, eds. T. Andersen, B. Fastrup, F. Folkmann and H. Knudsen (Aarhus, Denmark, 1993) p. 800.
98. R.W. Van Boeyen and J.F. Williams, in *XIX. Int. Conf. on the Physics of Electronic and Atomic Collisions, Abstracts*, eds. J.B.A. Mitchell, J.W. McConkey and C.E. Brion (Whistler, Canada, 1995) p. 504.
99. K. Yamazaki, A. Danjo, M. Yoshino, H. Tanuma and N. Kobayashi, in *XIX. Int. Conf. cn the Physics of Electronic and Atomic Collisions, Abstracts*, eds.

J.B.A. Mitchell, J.W. McConkey and C.E. Brion (Whistler, Canada, 1995) p. 809.
100. H. Hafner, J.A. Simpson and C.E. Kuyatt, Rev. Sci. Instr. **39**, 33 (1968).
101. J.S. Risley, Rev. Sci. Instr. **43**, 95 (1972).
102. E.M. Purcell, Phys. Rev. **54**, 818 (1938).
103. N. Stolterfoht, D. Schneider, D. Burch, B. Aagaard, E. Bøving and B. Fastrup, Phys. Rev. A **12** 1313 (1975).
104. N. Solterfoht, D. Schneider, D. Burch, H. Wiemann and J.S. Risley, Phys. Rev. Lett. **33**, 59 (1974).
105. A. ltoh, T. Schneider, G. Schiwietz, Z. Roller, H. Platten, G. Nolte, D. Schneider and N. Stolterfoht, J. Phys. B **16**, 3965 (1983).
106. D. Ridder, J. Dieringer and N. Stolterfoht, J. Phys. B **9**, L137 (1976).
107. D.L. Matthews, B.M. Johnson, J.J. Mackey, L.E. Smith, W. Hodge and G.F. Moore, Phys. Rev. A **10**, 1177 (1974).
108. E. Blauth, Z. Phys. **147**, 228 (1957).
109. L.H. Toburen, Phys. Rev. A **3**, 216 (1971).
110. D. Varga, Á. Kövér, L. Kövér and L. Redler, Nucl. Instr. Meth. A **238**, 393 (1985).
111. Á. Kövér, Gy. Szabó, D. Berényi, L. Gulyás, I. Cserny, K-O. Groeneveld, D. Hofmann and M. Burkhard, Phys. Rev. A **34**, 2751 (1986).
112. Á. Kövér, D. Varga, I. Cserny, E. Szmola, Gy. Mórik, L. Gulyás and K. Tokési, Nucl. Instr. Meth. A **373**, 51 (1996).
113. D. Varga, J. Végh, Á. Kövér, S. Ricz and A. Domonyi, Atomki Reports, **23**, 80 (1981).
114. D. Varga, I. Kádár, S. Ricz, J. Végh, Á. Kövér, B. Sulik and D. Berényi, Nucl. Instr. Meth. A **313**, 163 (1992).
115. A. Fahlmann, S. Hangstrom, K. Hamrin, R. Nordberg, C. Nordling and K. Siegbahn, Ark. Fys. **31**, 479 (1966).
116. D.A. Hutchital and J.D. Rigden, *Electron Spectroscopy*, (North Holland, Amsterdam, 1972) p. 79.
117. D.J. Lynch, L.H. Toburen and W.E. Wilson, J. Chem. Phys. **64**, 2616 (1976).
118. Gy. Vikor and S. Ricz, private communication.
119. D. Burch, N. Stolterfoht, D. Schneider, H. Wiemann and J.S. Risley, Nuclear Physics Annual Report 1974 (Univereity of Washington, Seattle, 1975) unpublished.
120. D. Schneider, C.F. Moore and B.M. Johnson, J. Phys. B **9**, L153 (1976).
121. D.F. Burch, in *Proc. Intern. Conf. on Inner-Shell Ionization Phenomena*, eds. R.W. Fink et al., Conf.-720 404 (USAEC, Oak Ridge, 1973).
122. J.M. Hansteen and O.P. Mosebeck, Phys. Rev. Lett. **29**, 1361 (1972).
123. B. Sulik, G. Hock and D. Berényi, J Phys. B **17**, 3239 (1984).
124. N. Stolterfoht, X. Husson, D. Lecler, R. Köhrbrück, B. Skogvall, S. Andriamonje and J.P. Grandin, in *XVII. Int. Conf. on the Physics of Electronic and Atomic Collisions, Abstracts*, eds. I.E. McCharty, W.R. McGillivray and M.C. Standage (Griffith University, Brisbane, Australia, 1991) p. 393.
125. E. Takács, S. Ricz, J. Végh, I. Kádár, J. Pálinkás, B. Sulik, L. Tóth, D.

Berényi and N.M. Kabachnik, Phys. Rev. A **50**, 1197 (1994).
126. A. Russek and W. Mehlhorn, J. Phys. B **19**, 911 (1986).
127. M.Yu. Kuchiev and S.A. Sheinerman, Sov. Phys.-JETP **63**, 986 (1986); Sov. Phys.-USP **32**, 596 (1989).
128. P. van der Straten and R. Morgenstern, J. Phys. B **19**, 1361 (1986).
129. P. van der Straten, R. Morgenstern and A. Niehaus, Z. Phys. D **8**, 35 (1988).
130. R.O. Barrachina and J.H. Macek, J. Phys. B **22**, 2151 (1989).
131. J.K. Swenson, C.C. Havener, N. Stolterfoht, K. Sommer and F.W. Meyer, Phys. Rev. Lett. **63**, 35 (1989).
132. S. Ricz, I. Kádár and J Végh, Nucl. Instr. Meth. B **40/41**, 77 (1989).